

## Unique trace element geochemistry of pyrometamorphic apatite-supergrout minerals: a case study of fluorellestadite from burnt coal (Poland) and shale (France) post-mining waste heaps, with emphasis on boron, germanium, aluminium and titanium

Łukasz KRUSZEWSKI<sup>1, \*</sup>, Jiří SLÁMA<sup>2</sup> and Ewa DEPUT<sup>1</sup>

- <sup>1</sup> Institute of Geological Sciences, Polish Academy of Sciences (IGS PAS), Twarda 51/55, 00-818 Warszawa, Poland; ORCID: 0000-0001-6332-9944 [L.K.]
- <sup>2</sup> Department of Geological Processes, Institute of Geology of the Czech Academy of Sciences, Rozvojová 269, 165 00 Praha 6 – Lysolaje, Czech Republic; ORCID: 0000-0002-1386-4196



Kruszewski, Ł., Sláma, J., Deput, E., 2023. Unique trace element geochemistry of pyrometamorphic apatite-supergrout minerals: a case study of fluorellestadite from burnt coal (Poland) and shale (France) post-mining waste heaps, with emphasis on boron, germanium, aluminium and titanium. *Geological Quarterly*, 67: 7, doi: 10.7306/gq.1677

Associate Editor: Tomasz Bajda

Apatite-type structure is known for its flexibility towards accommodating numerous ions of different crystallographic affinities. The trace element composition of two samples of fluorellestadite from pyrometamorphic rocks (slags) of burnt waste heaps (BWH) from France (LdS) and Poland (RDT) were studied using Laser Ablation Inductively Coupled Plasma Mass Spectrometry. Boron shows an evident, persistent enrichment in both samples, with average/maximum levels of 497/1040 and 49/106 ppm, respectively, as do magnesium (884/16766 and 404/6251 ppm, respectively) and sodium (512/697 and 249/370 ppm, respectively). Germanium is clearly enriched in the first sample (29/40 ppm) and, to a lesser degree, in the second one (34 ppm on average). The LdS sample is also clearly enriched in Al (888/1238 ppm), K (385/697 ppm), Ti (515/943 ppm), V (172/347 ppm), and Cu (16/1369 ppm). The RDT sample is also rich in As (105/120 ppm) and Sr (1072/6592 ppm). In the REE pattern of both samples, Nd dominates, with respective Nd/ LREE and Nd/(Ce+La) values of 0.43 and 0.90; and 0.37 and 0.66. From highest to lower average concentrations, aluminium, magnesium, titanium, boron, potassium and germanium may be essential substituents in the BWH apatites.

Key words: apatite supergroup, non-nominal ion substitution, boron, germanium, titanium, tetrahedra.

### INTRODUCTION

The apatite supergroup (ASG) is defined as minerals with the general formula  ${}^{\text{IX}}M1_2{}^{\text{VII}}M2_3({}^{\text{IV}}\text{TO}_4)_3X$  (Pasero et al., 2010). As such, this type of structure bears nonacoordinated (6+3; metaprism or tri-capped trigonal prism) *M1* sites, heptacoordinated (distorted pentagonal bipyramid) *M2* sites, tetrahedral *T* sites, and *X* sites mainly reserved for mono- and/or divalent anions. Typical residents of the *M* sites are  $\text{Ca}^{2+}$ ,  $\text{Sr}^{2+}$ ,  $\text{Ba}^{2+}$ ,  $\text{Pb}^{2+}$ ,  $\text{REE}^{3+}$  (REE – rare earth elements), and more rarely  $\text{Mn}^{2+}$ ,  $\text{Na}^+$ , and  $\text{Bi}^{3+}$ . The *M1* sites may sometimes be split into non-equivalent sites, and thus many apatite-structured compounds are crystallochemically far from the nominal ideal formula. Some such compounds show discrepancies from the above ideal stoichiometry, e.g., vanackerite,  $\text{Pb}_4\text{Cd}(\text{AsO}_4)_3\text{Cl}$ .

Pasero et al. (2010) report that, in addition to minerals, the *M* site may be occupied by K, Co, Cd, and most REEs, and the *T* site by Be, Cr,  $\text{Mn}^{5+}$ , and Ge in synthetic compounds. Nevertheless, the typical residents at the *T* site are  $\text{P}^{5+}$ ,  $\text{As}^{5+}$ ,  $\text{Si}^{5+}$ ,  $\text{S}^{6+}$ ,  $\text{V}^{5+}$ , and  $\text{B}^{3+}$ . The  $\text{PO}_4^{3-}$  anion may be partially protonated (e.g., Dordević et al., 2008), and a fraction of sulfur may be reduced to the +4 state (e.g., up to 100 ppm, Xu et al., 2020) or even the –2 (sulphide) state (Brounce et al., 2019; Xu et al., 2020). Boron-dominant apatite-supergrout minerals are, as yet, unknown. However, tritomite-(Ce) and tritomite-(Y) are sometimes placed within the group, with compositions such as  $\text{Ce}_{10}(\text{SiO}_4)_4(\text{BO}_4)_2\text{O}_2$  (Pan and Fleet, 2002). The *X* (channel) site is usually occupied by  $\text{F}^-$ ,  $\text{OH}^-$ ,  $\text{Cl}^-$ , but may also bear  $\text{O}^{2-}$ , and even trace  $\text{Br}^-$  (Dong, 2005) and  $\text{CN}^-$  (e.g., Broska et al., 2014) anions. The structural robustness and chemical diversity of “apatites” is well known to many authors (e.g., Hughes and Rakovan, 2015). In addition to natural ASG species, extensive diadochy is exploited in synthetic materials, too. This is especially important in the rapidly developing field of long-term storage of dangerous synthetic radionuclides – a feature also exploited in apatite-related studies (e.g., Moore et al., 2009; Wang

\* Corresponding author, e-mail: [lkruszewski@twarda.pan.pl](mailto:lkruszewski@twarda.pan.pl)

et al., 2015; Rigali et al., 2016), including sorption and formation of compounds of  $\text{CaPu}_4(\text{SiO}_4)_3\text{O}$  type (Villiers et al., 2015). Further examples include both stoichiometric and non-stoichiometric apatite-structured compounds with species-defining lithium, e.g.:  $\text{Li}_{0.5}\text{La}_{4.5}(\text{SiO}_4)_3\text{O}$ ; magnesium, e.g.,  $\text{Mg}_{0.25}\text{La}_{5.83}\text{Si}_{2.75}\text{O}_{13}$ ; manganese(V), e.g.,  $\text{Ba}_5\text{Mn}_{1.5}(\text{PO}_4)_{1.5}\text{ClO}_6$ ; iodine, e.g.,  $\text{Ca}_{15}(\text{PO}_4)_9\text{OI}$ ; vanadium and/or germanium, e.g.,  $\text{BaLa}_4\text{V}_{0.13}\text{Ge}_{2.88}\text{O}_{13.06}$ ,  $\text{PrPb}_4(\text{GeO}_4)_2(\text{VO}_4)$  (with empty channel sites), or  $\text{H}_{0.66}\text{Sr}_{2.66}\text{La}_{2.34}(\text{GeO}_4)_3(\text{OH})$ ;  $\text{Ca}_{4.24}\text{Co}_{0.75}(\text{PO}_4)_3(\text{OH})$ ; zinc, e.g.,  $\text{Sr}_{3.5}\text{Zn}_{1.4}(\text{PO}_4)_3\text{F}$ ; tin, e.g.,  $\text{K}_3\text{Sn}_2(\text{SO}_4)_3\text{Cl}$ ; rhenium, e.g.,  $\text{Ba}_5\text{Re}_3\text{O}_{15}(\text{OH})_{0.62}\text{I}_{0.39}$ ; sulphide-bearing  $\text{Sm}_{4.67}(\text{SiO}_4)_3\text{S}$  or  $\text{Ca}_{4.25}\text{Eu}_{0.75}(\text{PO}_4)_3\text{S}_{0.88}$ ; and even nitrogen-bearing species such as  $\text{La}_5\text{Si}_3\text{NO}_{12}$ . Boron-rich compounds include  $\text{Na}_{0.2}\text{Sr}_{9.4}\text{B}(\text{PO}_4)_6\text{O}_2$  and  $\text{La}_3\text{Eu}_2(\text{SiO}_4)_2\text{BO}_5$  (Villiers et al., 2015). Other ions known in the apatite-type compounds include  $[\text{BeF}_4]^-$ ,  $\text{Br}^-$ ,  $[(\text{Ge,C})(\text{O},\text{OH})_4]^{n-}$ ,  $\text{Cr}^{\text{VI}}\text{O}_4^{3-}$ ,  $\text{Cr}^{\text{VI}}\text{O}_4^{2-}$ ,  $\text{SeO}_4^{2-}$ ,  $\text{ReO}_5^{3-}$  and  $\text{OsO}_5^{3-}$ ,  $\text{SbO}_3\text{F}^{4-}$ ,  $\text{SiO}_3\text{N}^{5-}$ ;  $\text{K}^+$ ,  $\text{Rb}^+$ ,  $\text{NH}_4^+$ ,  $\text{Eu}^{2+}$ ,  $\text{Cr}^{3+}$ ,  $\text{U}^{4+}$  and  $\text{U}^{6+}$ . The *M* sites may also be partially vacant. Due to polysomatism towards nasonite,  $\text{Pb}_9\text{Ca}_4(\text{Si}_2\text{O}_7)_3$ , disilicate and digermanate anions seem possible, with symmetry lowering from  $P6_3/m$  to the *P*-6 space group (White and ZhiLi, 2003; Ptáček, 2016). To make the image even more complex, the channel sites may also bear  $\text{O}_2^-$  (superoxide),  $\text{O}_2^{2-}$  (peroxide),  $\text{O}_3^-$  (ozonide),  $\text{NCO}^-$  (cyanate),  $\text{NCN}^{2-}$  (carbodiimide),  $\text{BO}_2^-$  (metaborate),  $\text{NO}_2^-$  (nitrite),  $\text{NO}_2^{2-}$  (dioxidonitrate(2-)), and may also be partially vacant (Ptáček, 2016). Bostick et al. (2003) showed that apatites may be used to decontaminate some amounts of Cd, Cu, Hg, Mn, Zn, Sb and Se(IV). They report the following sorptive affinity for anions in their material:  $\text{VO}_4^{3-} > \text{MoO}_4^{2-} > \text{SeO}_3^{2-} > \text{AsO}_4^{3-} > \text{CrO}_4^{2-} > \text{TcO}_4^-$ ; and cations:  $\text{UO}_2^{2+} > \text{Pb}^{2+} > \text{Th}^{4+} > \text{Cd}^{2+} > \text{Mn}^{2+} > \text{Zn}^{2+} > \text{Cu}^{2+}$ ,  $\text{SbO}^+$  and  $\text{Hg}^{2+} > \text{Ni}^{2+} > \text{Sr}^{2+} > \text{Ba}^{2+}$ .

The ASG also shows interesting micro-scale crystallochemical phenomena, exploited by Fleet and Liu (2007, 2008). They described two types of diadochy of the  $\text{CO}_3^{2-}$  (carbonate) ions: type A, involving the channel (*X*) sites and coupled with Na substitution at the *M* sites; and type B, with carbonate occupying sloping faces of the *T*-site tetrahedra. Furthermore, the location of  $\text{CO}_3^{2-}$  ions nearby (*surplus*)  $\text{F}^-$  ions was observed by these and other (e.g., Regnier, 1996) authors. Another interesting nanoscale phenomenon is oxygen migration, observed for apatite-type lanthanum silicates (Liao et al., 2013).

Both boron and germanium are rare elements, at a few ppm crustal average (Parker, 1962). Germanium, along with Be, Bi, Co, Ga, Sc, W, V and REEs, is treated as a critical or strategic material (European Commission, 2017). Interestingly, Mg is included as one at the highest supply risk (Bowles et al., 2018). Even though the apatite-type structure is known to be capable of holding numerous elements and their forms, data on the concentrations of many elements is scarce. Examples of such data are given in Table 1.

The fluorellestadite-fluorapatite solid solution – rich in Si and S substituting for P – is a typical component of metacarbonate slags, a type of pyrometamorphic rock, or PM, formed by thermal transformation followed by decarbonisation of a carbonate-rich bituminous-shale protolith. As discussed by Ciesielczuk et al. (2015), pyrometamorphic ASG representatives may form at different temperatures (600 to >1200°C range). These authors were able to obtain fluorapatite, as a trace component of a periclase-srebrodolskite-portlandite-dominant product, after heating a dolomite-ankerite-quartz-kaolinite-(siderite-“illite”) gangue rock with a small addition of  $\text{CaF}_2$  flux. Apatite-type compounds are stable up to ~1600°C during coal ash fusion, the temperature where initial decomposition begins (Reifenstein et al., 1999).

Electron microprobe (EPMA) analysis of typically blue fluorellestadite-fluorapatite from a clinopyroxene-wollastonite-

anhydrite-rich metacarbonate slag of a waste heap at Lapanouse-de-Sévérac (Kruszewski et al., 2018a), suggested enrichment in Al, and possibly Mg. This led to a question: are these elements coming from tiny inclusions, or are contained within the structure? To provide answer, the sample was further analyzed using Laser Ablation Inductively Coupled Plasma Mass Spectrometry (LAICPMS). To check if the Mg- and Al-related phenomenon is restricted to this single sample or not, a comparative slag-derived sample from a burnt post-coal-mining waste heap in Rydułtowy (Upper Silesian Coal Basin, Poland) was analyzed, too. The resulting, unique geochemical/crystallochemical data is the matter of this paper. Another reason for undertaking this research is the idea of Re-Mining, i.e., extraction of (especially critical) raw materials from wastes, deposited in heaps and settling ponds (e.g., Blengini et al., 2019; Machiels and Perumal, 2022). Profound Re-Mining-related activities concern, in particular, Germany (e.g., EIT Raw Materials; Vrancken and Delgado, 2016), and encourage reconnaissance and search for new sources of rare elements.

## MATERIALS AND METHODS

The Lapanouse site is located in Sévérac-d’Aveyron, Rodez, Aveyron, Occitanie; 44°19’41” N, 3°2’43” E; and is herein referred as to LdS. The heap in Rydułtowy, known as “Szarłota”, is a large, typical coal-fire heap located in Wodzisław county, Silesian Voivodship (50°03’40” N, 18°26’32” E; herein referred as to RDT; Kruszewski, 2008). The parent slag from LdS bears leucite, anorthite, and orthoclase/sanidine in addition to the major species noted above. Accessory minerals in the LdS slag include magnesioferrite ( $\text{Mg-Fe}^{3+}$  oxyspinel) and srebrodolskite (a Ca ferrite,  $\text{Ca}_2\text{Fe}_2\text{O}_5$ ; e.g., Kruszewski, 2008). The fluorellestadite-rich marginal zones have anhydrite as a major and gypsum as a minor phase (Fig. 1A). In other slag samples, geochemically and crystallochemically exotic apatite-supergroup species occur, including (Sr,V)-enriched fluorellestadite (2% of the pliniusite,  $\text{Ca}_5(\text{VO}_4)_3\text{F}$ , end member), and a (Sr,Cr,P,Si)-rich V-dominant species (pliniusite) with up to 23.67 wt.%  $\text{V}_2\text{O}_5$  (1.64 V atoms per formula unit, *apfu*) and up to 0.55 wt.%  $\text{CrO}_3$  (0.14 *apfu* Cr; Kruszewski et al., 2018a). Maximum  $\text{TiO}_2$  and  $\text{Al}_2\text{O}_3$  contents in this species are 3.81 and 0.49 wt.%, respectively. The average composition of the French fluorellestadite analysed is [wt.%, EPMA]:  $\text{SO}_3$  12.51–20.18 (geometric mean, i.e., GM, of 16.48),  $\text{P}_2\text{O}_5$  0.17–3.28 (GM=0.58),  $\text{SiO}_2$  17.56–23.09 (GM=19.76),  $\text{Al}_2\text{O}_3$  below the detection limit (bdl) – 1.56,  $\text{FeO}$  bdl–0.43,  $\text{MgO}$  bdl (single case: 0.06),  $\text{CaO}$  56.48–61.27 (GM=59.63),  $\text{F}$  1.50–2.89 (GM=2.20),  $\text{H}_2\text{O}$  (by difference) 0.32–0.97 (GM=0.59). The likely empirical formula is  $\text{Ca}_{5.00}[(\text{SiO}_4)_{1.55}(\text{SO}_4)_{0.92}(\text{PO}_4)_{0.03}(\text{AlO}_4)_{0.02}(\text{CO}_3)_{0.51}]_{3.01}[\text{F}_{0.55}(\text{OH})_{0.30}]_{0.85}$ , corresponding to 61% of fluorellestadite, 35% of hydroxyllestadite, 2% of a hypothetical Al-dominant apatite, 1% of fluorapatite, and 1% of hydroxylapatite end-member. The average composition of the Rydułtowy (RDT) material is [wt.%, EPMA]:  $\text{SO}_3$  8.34–18.19 (GM=13.14),  $\text{P}_2\text{O}_5$  3.90–21.88 (GM=9.63),  $\text{SiO}_2$  8.73–18.66 (GM=13.54),  $\text{FeO}$  bdl–1.24,  $\text{SrO}$  bdl (single case: 0.47),  $\text{MgO}$  bdl (single case: 0.08),  $\text{CaO}$  54.84–58.49 (GM=56.84),  $\text{F}$  3.60–4.85 (GM=4.02). It is associated with srebrodolskite and magnesioferrite (Fig. 1B). The empirical formula is  $(\text{Ca}_{4.98}\text{Fe}_{0.02})_{5.00}[(\text{SiO}_4)_{1.11}(\text{SO}_4)_{0.81}(\text{PO}_4)_{0.67}(\text{CO}_3)_{0.45}]_{3.04}\text{F}_{1.04}$ , corresponding to 45% of fluorellestadite, 33% of a carbonate-dominant analogue of fluorellestadite, and 22% of fluorapatite end-member composition (Kruszewski, 2008; Ciesielczuk et al., 2015).

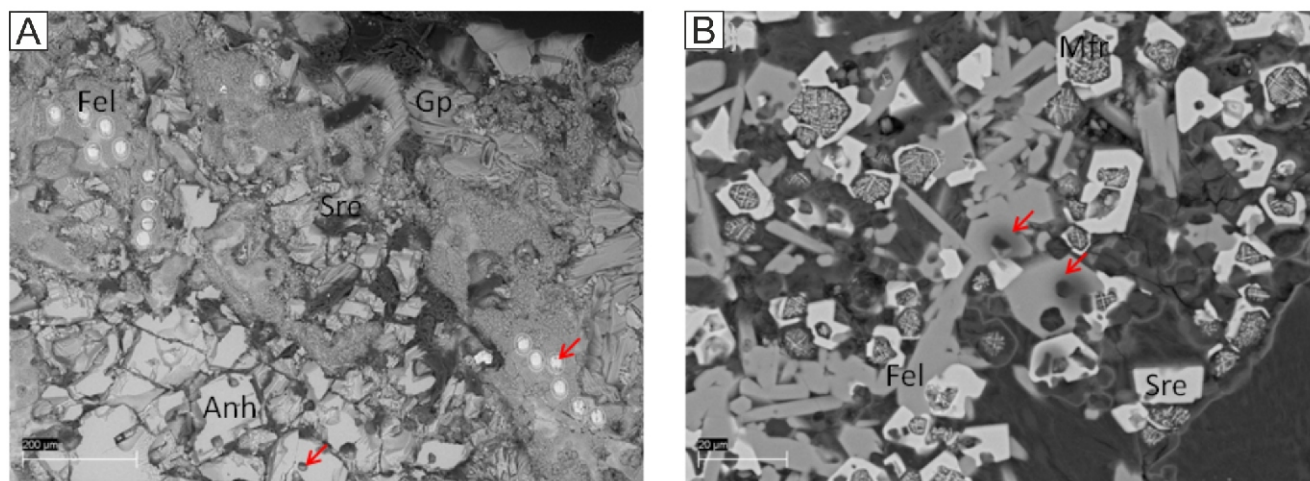
Laser Ablation Inductively-Coupled Plasma Mass Spectrometry (LAICPMS) was used to obtain data on the trace ele-

Table 1

Average concentrations of some trace elements (ppm) in apatites and phosphorites (given in italics)

Examples	1	2	3	4	5	6	7	8	9	10	11	12	13	14	15	GM
Al	0.01 <sup>1</sup>	58 <sup>2</sup>	6900 <sup>14</sup>	106 <sup>17</sup>												26
As	35 <sup>3</sup>	20 <sup>1</sup>	6.7 <sup>4</sup>	22 <sup>5</sup>	148 <sup>6</sup>	12 <sup>7</sup>	532 <sup>8</sup>	97150 <sup>15</sup>	265 <sup>19</sup>	210 <sup>20</sup>	197 <sup>21</sup>					60
B	330 <sup>7</sup>															
Co	145 <sup>9</sup>	6.6 <sup>7</sup>	66 <sup>8</sup>	0.35 <sup>11</sup>	12 <sup>19</sup>	17 <sup>20</sup>	8 <sup>21</sup>									9.6
Cr	1.6 <sup>2</sup>	267 <sup>9</sup>	176 <sup>7</sup>	1058 <sup>8</sup>	1.2 <sup>11</sup>											7.3
Cs	1.1 <sup>8</sup>	0.03 <sup>16</sup>	5.0 <sup>19</sup>	0.1 <sup>20</sup>	5.8 <sup>21</sup>											0.54
Cu	0.2 <sup>4</sup>	(4.2) <sup>2</sup>	32 <sup>9</sup>	2.4 <sup>3</sup>	2 <sup>7</sup>	13 <sup>8</sup>	30 <sup>19</sup>	21 <sup>20</sup>	24 <sup>21</sup>							7.2
Fe	117 <sup>3</sup>	318 <sup>1</sup>	6.7 <sup>4</sup>	800 <sup>4</sup>	708 <sup>5</sup>	1138 <sup>6</sup>	~500 <sup>10</sup>	2700 <sup>12</sup>	1900 <sup>14</sup>	38100 <sup>15</sup>	932 <sup>17</sup>	777 <sup>18</sup>	4608 <sup>19</sup>	4480 <sup>20</sup>	1869 <sup>21</sup>	727
Ga	32 <sup>11</sup>	17 <sup>2</sup>	~75 <sup>10</sup>	2 <sup>9</sup>	33 <sup>8</sup>	22 <sup>19</sup>	14 <sup>20</sup>	14 <sup>21</sup>								17
Ge	25 <sup>11</sup>	17 <sup>6</sup>	2 <sup>9</sup>	20 <sup>8</sup>												9.5
K	22 <sup>6</sup>	1660 <sup>15</sup>														
Li	4 <sup>11</sup>															
Mg	116 <sup>3</sup>	32 <sup>1</sup>	68 <sup>4</sup>	209 <sup>6</sup>	600 <sup>14</sup>	2350 <sup>15</sup>	121 <sup>18</sup>	415 <sup>19</sup>	745 <sup>20</sup>	458 <sup>21</sup>						182
Na	1532 <sup>6</sup>	~290 <sup>10</sup>	1500 <sup>14</sup>	28900 <sup>15</sup>	1340 <sup>17</sup>	297 <sup>19</sup>	445 <sup>20</sup>	1261 <sup>21</sup>								762
Nb	(0.06) <sup>4</sup>	1.9 <sup>8</sup>	(5.0) <sup>13</sup>	0.03 <sup>16</sup>	8.1 <sup>19</sup>	19 <sup>20</sup>	3.0 <sup>21</sup>									1.3
Ni	0.94 <sup>3</sup>	3.1 <sup>6</sup>	26 <sup>7</sup>	90 <sup>8</sup>	1.6 <sup>11</sup>	43 <sup>19</sup>	48 <sup>20</sup>	34 <sup>21</sup>								8.3
Pb	10 <sup>1</sup>	8.6 <sup>5</sup>	7.4 <sup>7</sup>	56 <sup>8</sup>	231000 <sup>15</sup>	1.5 <sup>16</sup>	9 <sup>19</sup>	6 <sup>20</sup>	7 <sup>21</sup>							6.0
Rb	0.3 <sup>4</sup>	0.31 <sup>6</sup>	0.23 <sup>3</sup>	0.15 <sup>16</sup>												0.24
Sb	0.05 <sup>11</sup>	1.6 <sup>7</sup>														
Sc	0.04 <sup>4</sup>	36 <sup>9</sup>	26 <sup>8</sup>	44 <sup>19</sup>	32 <sup>20</sup>	25 <sup>21</sup>										7.4
Sn	2.3 <sup>12</sup>	0.88 <sup>7</sup>	10 <sup>8</sup>	16 <sup>19</sup>	28 <sup>20</sup>	12 <sup>21</sup>										11
Ti	0.01 <sup>1</sup>	1587 <sup>9</sup>	387 <sup>19</sup>	618 <sup>20</sup>	129 <sup>21</sup>											55
U	16 <sup>3</sup>	6.6 <sup>4</sup>	60 <sup>5</sup>	1.2 <sup>13</sup>	20 <sup>11</sup>	33 <sup>12</sup>	27 <sup>6</sup>	~40 <sup>10</sup>	82 <sup>7</sup>	86 <sup>8</sup>	318 <sup>15</sup>	11 <sup>16</sup>	14 <sup>19</sup>	9 <sup>20</sup>	10 <sup>21</sup>	14
V	7.7 <sup>3</sup>	9.2 <sup>1</sup>	8.8 <sup>4</sup>	9.8 <sup>5</sup>	22 <sup>11</sup>	38 <sup>6</sup>	12 <sup>2</sup>	7.7 <sup>9</sup>	121 <sup>7</sup>	295 <sup>8</sup>	8960 <sup>15</sup>	17 <sup>19</sup>	26 <sup>20</sup>	14 <sup>21</sup>		14
Zn	3.4 <sup>3</sup>	1.4 <sup>4</sup>	20 <sup>9</sup>	20 <sup>7</sup>	482 <sup>8</sup>	126 <sup>19</sup>	116 <sup>20</sup>	98 <sup>21</sup>								23
Zr	2.6 <sup>3</sup>	0.1 <sup>4</sup>	8.6 <sup>13</sup>	108 <sup>9</sup>	0.72 <sup>16</sup>	34 <sup>18</sup>	21 <sup>19</sup>	25 <sup>20</sup>	5 <sup>21</sup>							6.3

Data given in parentheses represent exemplary concentration (with typical values below detection limits); GM – geometric mean (excluding data for phosphorites – Bech et al., 2010) and Bishady et al. (2019) – and extreme levels (Chakmouradian et al., 2017); <sup>1</sup> Belousova (2001), granitoids; <sup>2</sup> Pan et al. (2021), Cu-Au porphyry deposits and granitoids; <sup>3</sup> Belousova (2002), igneous rocks; <sup>4</sup> Mao et al. (2016), Cu-Au porphyry deposits; <sup>5</sup> Sha and Chappell (1999), granitoids; <sup>6</sup> La Cruz et al. (2020), Fe-oxide-apatite deposit; <sup>7</sup> Bech et al. (2010), phosphorites; <sup>8</sup> Bishady et al. (2019), Egyptian phosphorites; <sup>9</sup> Mason and Graham (1970), phosphates in meteorites; <sup>10</sup> Zhang et al. (2020), Au-bearing mineralization; <sup>11</sup> Duan and Jiang (2018), ore deposits and granitoids; <sup>12</sup> Azadbakht et al. (2018), granitoids; <sup>13</sup> Tollari et al. (2008), intrusive rocks; <sup>14</sup> Guo et al. (2014), phosphate deposits of Northern China; <sup>15</sup> Chakmouradian et al. (2017), non-biogenic apatites, extreme levels; <sup>16</sup> Kimura (2000), Durango apatite; <sup>17</sup> Xiqiang et al. (2020); <sup>18</sup> Schleicher et al. (2019), carbonatites; <sup>19</sup> Mercer et al. (2019), rhyolite suite; <sup>20</sup> Mercer et al. (2019), mafic/intermediate suite; <sup>21</sup> Mercer et al. (2019), Fe ores and their host



**Fig. 1.** Backscatter-electron images of individual fluorellestadite (Fel) crystals within matrices of the two slag samples comprising anhydrite (Anh), gypsum (Gp), magnesioferrite (Mfr) and srebrodolskite (Sre)

**A** – LdS sample; **B** – RDT sample; the red arrows point to craters due to the LAICPMS

ment composition of the samples. The analyses were conducted using a Thermo Scientific Element 2 sector field ICPMS coupled with 193 nm ArF excimer laser (Teledyne Cetac Analyte Excite laser), located at the Institute of Geology, Czech Academy of Sciences, Prague. The laser energy was 5.7 J/cm<sup>2</sup>, repetition rate was 5 Hz, flow of the He carrier gas was 765 ml/min. The analyses' timing was: 20 s of gas blank, 35 s of ablation, and 30 s of cell wash-out. The in-house glass signal homogenizer (design of Tunheng and Hirata, 2004) was used for mixing all the gases and aerosol resulting in a smooth, spike-free signal. The signal was tuned for maximum sensitivity while keeping low oxide level, commonly <0.1%. The beam size was minimized to meet the diameters of the crystals studied; it was 20 μm in the case of the larger LdS crystals, and 13 μm in the case of the RDT ones. After the LAICPMS session the thin sections were observed using a Scanning Electron Microscope to confirm that all the post-analytical holes were localized directly within the fluorellestadite crystals. The measurement sequence consisted of repeated blocks of 2 analyses of NIST SRM610, one analysis of BCR-2 standard and 10 unknowns. The dead-time corrected trace element data were calibrated against NIST SRM610 glass. The minimum detection limit values were calculated by multiplying the variance of the background by 3.25 for individual elements and are listed in the data table. The time-resolved signal data were processed using Glitter software (van Achterbergh et al., 2001). In total, 29 crystals from LdS and 17 crystals from RDT were analysed. This gives 47 analyses (Tables 2 and 3), one analysis per each crystal.

## RESULTS

### TRACE-ELEMENT COMPOSITION OF THE FLUORELLESTADITES

The LdS15 fluorellestadite sample is very rich in terms of both the number of enriched elements and their contents (Table 2). The most evident, intense enrichment are seen in (average/maximum) B 497/1040, Na 512/697, Mg 885/16766, Al 888/1238, K 385/697, Ti 515/943, V 172/347, Cu 16/1369 and Ge 29/40. Compared to the average contents calculated for published data for variable-provenience apatites (Table 1), the contents in LdS15 are ~5 times higher for Mg, 34 times

higher for Al, >9 times higher for Ti, 12 times higher for V, >2 times higher for Cu and 3 times higher for Ge. There is less pronounced enrichment of As (61/114), Li (15/21), Cr (27/48), Mn (423/641), Fe (243/843), Zn (16/130) and W (0.90/11). Contents of other elements are moderate or low: Sc 2.1/4.4, Sr 88/205, Y 52/100, Zr 0.46/2.4, Nb 0.56/1.8, Ba 46/226, La 10/24, Ce 12/22, Pr 4.0/6.7, Nd 20/31, Sm 5.3/7.0, Eu 1.4/2.0, Gd 7/11, Dy 7/13, Tb 1.1/1.9, Er 4.0/8.1, Ho 1.5/2.9, Tm 0.51/1.1, Yb 3.0/6.2, Lu 0.45/0.96, Pb 5.0/9.7, Th 0.49/2.5 and U 0.14/2.5. Cobalt and nickel are found only occasionally.

The number of positively determined trace-element concentrations in the sample RDTb16c fluorellestadite is much lower (Table 3). Nevertheless, its crystals are clearly enriched in Sr (1072/6592), B (49/106), Mg (404/6251), Na (249/379), Ge (34/37; fewer positive records than in the LdS15 material), and As (105/120). They show lower contents of V (16/23), Ge (13/25), Y (38/72), Ba (8.4/25), Dy (5.4/11), Er (1.9/3.3), Ho (1.0/1.5), Tm (0.28/0.34) and Yb (1.0/1.9), though clearly higher contents of La (18/45), Ce (29/56), Pr (6.2/17), Nd (31/89), Sm (12/23), Eu (2.6/5.5) and Gd (13/25). Pb is found occasionally, with the maximum level of 1.1 ppm.

The average total REE content in the LdS15 and RDTb16c fluorellestadite is 134 and 155 ppm, respectively. The LdS15 material is HREE-dominant (GM=71 ppm), relative to its LREE (GM=46 ppm) and MREE (GM=14 ppm) contents. The RDTb16c crystals are LREE-dominant, at GM=85 ppm, relative to its MREE (GM=28 ppm) and HREE (GM=47 ppm) contents. However, the common, interesting characteristics of both samples is their Nd dominance over the remaining REEs, as shown by the respective Nd/ LREE and Nd/(Ce+La) values of 0.43 and 0.90; and 0.37 and 0.66.

### STATISTICAL ANALYSIS

A mean-and-whisker plot for the LdS15 fluorellestadite (Fig. 2) shows the highest data spread for copper, followed by zinc, magnesium, uranium, barium, and tungsten. Lower spreads are shown by neodymium, praseodymium, samarium, europium, manganese; chromium, vanadium, potassium, arsenic, strontium and zinc. Low to moderate variation is found for gadolinium, terbium, titanium, sodium and HREEs. In the Shapiro-Wilk test (Table 4), only the praseodymium data shows

Table 2

Average concentrations of some trace elements (ppm) in fluorapatite-fluorellestadite from Lapanouse-de-Sévérac

	1	2	3	4	5	6	7	8	9	10	11	12	13	14	15
Li <sup>1</sup>	17	14	18	38	20	<b>21</b>	19	18	17	20	19	9.4	15	15	13
B	478	472	516	272	439	564	596	652	659	605	617	314	632	542	618
Na	696	531	612	356	661	681	<b>697</b>	666	650	633	647	338	576	569	550
Mg	2082	14641	4710	<b>16766</b>	821	1304	1537	770	547	864	576	265	845	368	470
Al	1238	451	737	761	881	1107	934	1072	974	1353	1173	492	1029	1137	892
K	402	346	412	238	406	574	405	483	413	376	428	328	442	394	400
Sc	1.6	<b>4.4</b>	2.6	1.5	1.6	2.1	2.7	2.6	2.3	1.2	1.7	1.0	2.5	1.7	3.0
Ti	296	262	288	189	481	627	552	648	566	689	646	336	674	654	625
V	226	<b>347</b>	305	210	124	152	175	143	154	115	127	287	146	144	154
Cr	19	37	31	25	30	22	25	24	26	21	23	27	23	26	27
Mn	287	<b>641</b>	577	583	456	464	428	393	421	408	413	396	372	436	373
Fe	249	521	331	612	402	255	210	160	188	267	232	182	198	212	135
Co	bdl <sup>2</sup>	15	bdl	5.8	bdl	bdl	bdl	bdl	bdl	bdl	bdl	bdl	bdl	bdl	bdl
Ni	bdl	58	bdl	24	bdl	bdl	bdl	bdl	bdl	bdl	bdl	bdl	bdl	bdl	bdl
Cu	38	<b>1369</b>	117	210	5.9	79	52	30	5.4	3.3	5.3	9.1	14	4.4	4.6
Zn	14	109	33	<b>130</b>	28	5.4	7.9	bdl	bdl	bdl	bdl	bdl	8.9	6.4	5.8
Ge	21	22	21	18	26	31	30	31	33	30	32	24	35	31	33
As	<b>114</b>	79	107	67	55	54	55	53	55	46	50	111	51	55	53
Sr	99	94	133	<b>205</b>	132	77	88	79	74	70	75	86	88	82	86
Y	32	56	56	30	34	50	61	53	55	31	40	51	56	55	82
Zr	0.32	0.40	0.54	0.38	0.58	0.39	0.47	0.47	0.30	0.33	0.33	0.41	0.45	0.35	0.46
Nb	0.34	0.34	0.56	0.26	0.44	0.57	0.61	0.69	0.55	0.63	0.63	0.53	0.68	0.59	0.62
Ba	45	21	76	<b>226</b>	37	63	112	52	38	35	43	21	51	32	51
La	<b>24</b>	16	22	14	7.0	8.4	8.3	8.4	8.3	8.4	8.6	16	9.0	9.5	9.8
Ce	<b>22</b>	12	20	13	5.2	7.7	6.5	7.0	7.2	7.4	7.2	18	11	9.5	12
Pr	6.2	4.6	<b>6.7</b>	4.1	2.9	3.5	3.3	3.4	3.7	3.5	3.6	4.8	4.0	4.0	4.1
Nd	28	34	<b>31</b>	19	14	19	19	19	19	17	18	22	21	19	20
Sm	5.3	5.9	<b>7.0</b>	4.3	3.7	5.2	5.4	5.2	5.6	4.3	4.7	5.0	5.0	5.0	6.5
Eu	1.3	1.6	<b>2.0</b>	1.1	1.2	1.3	1.5	1.4	1.3	1.0	1.1	1.5	1.4	1.4	1.9
Gd	5.6	8.3	9.7	6.2	4.7	6.7	8.2	6.9	7.4	4.4	5.6	7.1	7.1	7.3	10
Tb	0.71	1.2	1.3	0.75	0.73	1.1	1.2	1.1	1.2	0.71	0.78	1.0	1.1	1.2	1.6
Dy	4.3	7.6	7.9	4.1	5.2	6.8	8.7	7.2	7.6	4.3	5.3	6.8	7.5	6.9	11
Ho	0.95	1.5	1.5	0.81	1.0	1.4	1.7	1.6	1.6	1.0	1.0	1.4	1.6	1.6	2.5
Er	2.3	3.8	3.8	1.8	2.8	3.7	4.7	4.2	4.1	2.2	3.0	3.8	4.5	4.1	6.7
Tm	0.29	0.47	0.45	0.19	0.33	0.51	0.62	0.55	0.59	0.27	0.39	0.49	0.57	0.48	0.92
Yb	1.5	2.8	2.9	1.1	2.3	2.9	3.5	3.2	3.4	1.5	2.1	3.1	3.6	3.0	5.4
Lu	0.25	0.41	0.35	0.19	0.32	0.44	0.46	0.48	0.53	0.25	0.28	0.44	0.49	0.45	0.88
W	1.1	<b>11</b>	1.8	1.8	0.24	1.1	1.3	0.64	0.50	0.59	0.42	0.47	0.67	0.49	0.58
Pb	7.5	7.4	7.0	2.8	8.2	6.0	7.6	<b>9.7</b>	7.9	6.2	8.3	3.7	8.7	4.5	7.8
Th	<b>3.4</b>	1.4	2.5	1.5	0.23	0.33	0.33	0.27	0.33	0.26	0.30	1.4	0.38	0.35	0.35
U	bdl	0.13	0.44	0.07	0.06	0.15	0.32	0.22	0.23	0.27	0.07	bdl	0.11	0.05	0.08
	16	17	18	19	20	21	22	23	24	25	26	27	28	29	GM
Li	16	14	15	16	13	11	10	11	14	13	15	14	9.7	16	15
B	<b>1040</b>	667	629	501	335	361	329	380	587	673	746	697	243	132	492
Na	462	581	613	596	498	385	367	406	577	625	494	592	290	158	512
Mg	523	354	1543	1423	4184	291	283	206	710	535	632	437	322	inc <sup>3</sup>	884
Al	290	1081	1072	1335	855	811	786	853	999	1031	767	1023	<b>23375<sup>4</sup></b>	322	857
K	366	418	407	435	<b>697</b>	334	329	365	412	422	427	412	301	149	385
Sc	2.3	2.4	2.7	1.6	bdl	bdl	bdl	bdl	bdl	bdl	bdl	bdl	bdl	bdl	(2.1)
Ti	436	697	674	707	576	593	554	551	<b>943</b>	673	612	663	608	173	515
V	260	163	161	142	197	173	166	174	184	152	138	154	156	140	172
Cr	<b>48</b>	25	26	22	32	33	29	28	36	30	32	33	25	14	27
Mn	510	346	368	453	484	465	420	438	605	354	458	346	401	243	423
Fe	94	180	188	338	280	198	179	140	463	153	164	188	<b>843</b>	515	243
Co	bdl	bdl	bdl	bdl	bdl	bdl	bdl	bdl	bdl	bdl	bdl	bdl	bdl	bdl	inc
Ni	bdl	bdl	bdl	bdl	bdl	bdl	bdl	bdl	bdl	bdl	bdl	bdl	bdl	bdl	
Cu	32	3.8	15	9.8	103	5.5	6.6	4.6	17	6.2	11	7.1	3.3	94	16
Zn	5.6	bdl	9.8	12	49	bdl	bdl	bdl	bdl	bdl	9.4	bdl	bdl	30	(16)
Ge	32	31	32	33	31	32	29	31	35	31	<b>40</b>	32	32	13	29
As	73	52	52	52	65	65	57	60	60	51	58	50	60	59	61
Sr	79	80	89	83	130	76	79	78	84	82	88	82	86	57	88
Y	<b>100</b>	64	72	36	56	69	61	69	66	77	47	73	45	22	52
Zr	1.3	0.56	0.71	0.93	0.26	0.32	0.41	0.38	<b>2.4</b>	0.42	0.34	0.44	0.25	bdl	0.46
Nb	0.46	0.65	0.72	0.75	0.48	0.65	0.59	0.59	<b>1.8</b>	0.65	0.53	0.64	0.54	0.27	0.56
Ba	35	41	57	36	219	30	75	32	99	53	40	36	37	4.9	46
La	9.1	9.3	9.7	10	9.5	10	8.9	10	11	11	11	11	10	8.2	10
Ce	17	12	12	10	13	14	11	10	20	16	19	16	12	13	12
Pr	3.6	4.1	4.0	4.1	3.8	4.0	3.9	4.1	4.4	4.3	4.4	4.5	3.7	2.5	4.0
Nd	20	20	21	20	18	20	20	21	22	23	19	22	17	11	20
Sm	6.5	6.0	6.1	4.8	4.9	6.1	5.3	6.4	6.1	6.4	5.3	6.2	4.5	3.0	5.3
Eu	1.8	1.5	1.5	1.2	1.4	1.4	1.4	1.5	1.5	1.6	1.4	1.7	1.1	0.73	1.4

Tabl. 2 cont.

Gd	<b>11</b>	7.2	8.7	5.0	6.8	8.9	8.0	8.8	8.1	8.7	5.8	8.4	5.9	3.5	7.0
Tb	<b>1.9</b>	1.3	1.4	0.81	1.2	1.3	1.3	1.4	1.3	1.6	1.0	1.4	0.92	0.50	1.1
Dy	<b>13</b>	8.3	9.7	4.6	7.7	9.6	8.2	9.5	8.6	10	6.5	9.8	6.3	2.6	7.0
Ho	<b>2.9</b>	1.8	2.3	0.93	1.7	2.0	1.6	2.1	1.9	2.2	1.6	2.1	1.2	0.54	1.5
Er	<b>8.1</b>	5.0	6.3	2.3	4.8	5.2	4.6	5.8	5.1	6.5	3.9	5.8	3.6	1.4	4.0
Tm	<b>1.1</b>	0.68	0.73	0.33	0.60	0.64	0.61	0.67	0.67	0.84	0.59	0.75	0.48	0.18	0.51
Yb	<b>6.2</b>	4.2	4.8	1.7	3.5	4.2	3.5	4.5	4.1	5.2	3.5	4.9	2.6	1.1	3.0
Lu	<b>0.96</b>	0.64	0.71	0.28	0.48	0.56	0.51	0.61	0.64	0.77	0.55	0.75	0.37	0.15	0.45
W	2.5	0.62	1.1	0.66	2.1	0.62	0.73	0.45	inc	0.94	0.62	0.79	2.5	0.95	0.90
Pb	4.6	7.1	6.9	5.0	2.7	2.3	2.3	3.1	4.9	7.3	7.4	7.0	1.8	0.66	5.0
Th	0.42	0.40	0.47	0.43	0.33	0.46	0.39	0.42	0.40	0.45	0.30	0.38	0.43	0.60	0.49
U	0.26	0.10	0.07	0.10	0.11	bdl	bdl	bdl	<b>2.5</b>	0.07	bdl	0.07	0.16	bdl	0.14

GM – geometric mean; maximum levels are given in bold;<sup>1</sup> Be, Rb, Sn, Hf, and Ta were below their detection limits; <sup>2</sup> below detection limit; <sup>3</sup> inclusion; <sup>4</sup> possible contamination/inclusion

both normal distribution and  $\alpha = 0.05$ . Based on the theoretical Shapiro-Wilk  $W$  statistics values, 17 of 39 measured concentrations (44% of them) show a normal distribution.

The positive Kendall correlations (Table 5), with  $\alpha = 0.05$  are:

- 0.90: Y-Tb to Y-Er, Ho-Er, Ho-Tm, Er-Tm, Er-Yb, Tm-Yb, Tm-Lu, Yb-Lu;
- 0.75 < 0.90: Y-Gd, Y-Tm to Y-Lu, La-Nd, Sm-Eu, Sm-Tb, Gd-Tb, Gd-Dy, Tb-Dy to Tb-Yb, Dy-Ho to Dy-Lu, Ho-Yb, Ho-Lu, Er-Lu;
- 0.50 < 0.75: Li-Na, Na-Pb, Mg-Cu, Mg-Zn, Al-Ti, Sc-Y, Sc-Sm to Sc-Tm, Ti-Ge, Ti-Nb, V-As, Cr-Eu, Cr-Gd, Fe-Zn, Cu-W, Zn-Sr, Y-Sm, Y-Eu, La-Ce, La-Pr, La-Th, Ce-Pr, Ce-Nd, Ce-Th, Pr-Nd, Nd-Sm, Nd-Eu, Sm-Gd, Sm-Ho to Sm-Lu, Eu-Gd to Eu-Lu, Gd-Ho to Gd-Lu, Tb-Lu;
- 0.30 < 0.50: Li-Mg, B-Na, B-K, B-Ti, B-Y, B-Nb, B-Sm to B-Lu, B-Pb, Na-Mg, Na-Al, Na-K, Mg-Fe, Mg-Ba, Mg-W, Al-Nb, K-Ti, K-Ge, K-Nb, K-Ba, K-Pb, Sc-Yb, Sc-Lu, Sc-W, V-Cr, V-Cu, V-Sr, V-La to V-Gd, V-W, Cr-Mn, Cr-Y, Cr-Ce, Cr-Nd, Cr-Sm, Cr-Tb to Cr-Lu, Mn-As, Cu-As, Cu-Sr, Zn-As, Ge-Nb, Ge-Ho to Ge-Lu, As-La, As-Ce, As-Th, Sr-La, Sr-Pr, Y-Nb, Y-Nd, Zr-Nb, Zr-Eu, Nb-Dy to Nb-Lu, Ba-W, La-Gd, Ce-Sm, Ce-Eu, Pr-Sm, Pr-Eu, Pr-Th Nd-Gd to Nd-Er, Nd-Yb, Nd-Lu, Nd-Th, W-Th.

Other relatively strong positive correlations ( $\alpha = 0.30$ ,  $p > 0.05$ ) are found for the following pairs: B-Sc, Sc-Pb, Zn-La and Y-Nd.

The negative Kendall correlations, with  $\alpha = 0.05$ , are:

- 0.50 < 0.75: Ti-As, Fe-Ho to Fe-Lu;
- 0.30 < 0.50: Li-Y, Li-La, Li-Tb to Li-Lu, B-Fe, B-Zn, B-As, Na-Ce, Na-Th, Mg-Tm to Mg-Lu, Al-Sc, Al-V, Al-Cr, Al-Mn, Al-Cu, Al-As, Al-Eu, Al-Gd, K-As, K-Th, Ti-V, Ti-Cu, Ti-Zn, Fe-Sm to Fe-Dy, Zn-Ge, Zn-Y, Zn-Tb, Zn-Ho to Zn-Lu, Ge-As, As-Nb, Pb-Th.

The PCA allows pinpointing of collinear vectors (Fig. 3). They include the following groups:

- Yb, Lu, Tm, Er, B, K; Ho, Dy, Tb (somewhat negatively correlated with Fe);
- Pb, Gd, Sm, Eu, Nd;
- Cr, U (Ba);
- Ce, Mn, P, (Sc);
- Mg, As, La (somewhat negatively correlated with Ti);
- Th, Sr (somewhat negatively correlated with Ti);
- Zn, Li (negatively correlated with Ti);
- and Nb, Ge (negatively correlated with Fe)

Aluminium shows clear negative correlation with V, and to some extent with W, Ba, and the Ce+Mn+P group. The large Cu and Mg variation shown in the mean-and-whisker diagram is also clear in the PCA, as derived from the considerable length of their corresponding vectors.

A mean-and-whisker plot for the RDTb16c fluorellestadite (Fig. 4) differs somewhat from that of LdS15. It shows the highest data spread for magnesium, praseodymium, neodymium; strontium, yttrium, lanthanum, cerium, barium, uranium and

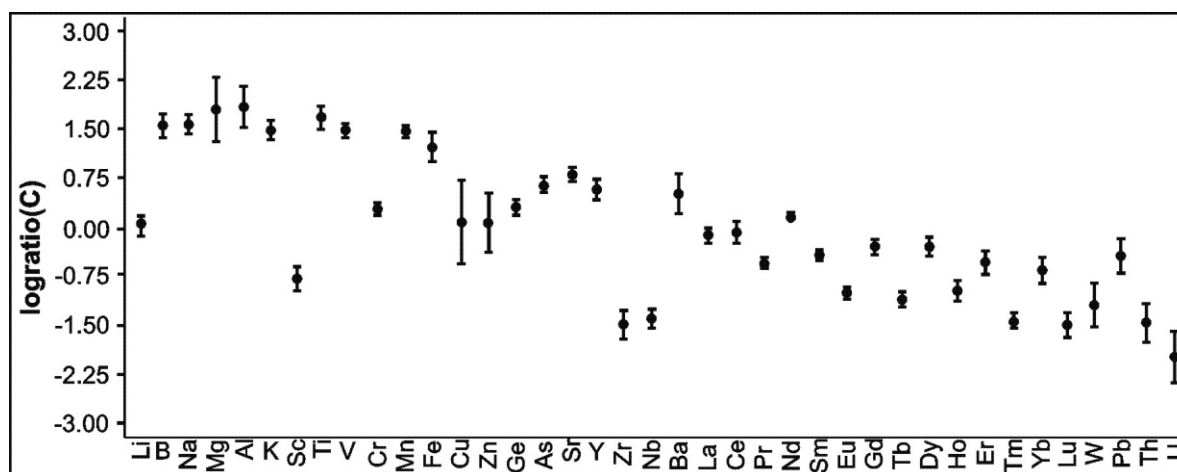


Fig. 2. Mean-and-whisker diagram of element-compositional data variation; the LdS15 post-oil-shale fluorellestadite sample, PAST software (Hammer et al., 2001) applied

Table 3

Average concentrations of trace elements (ppm) in fluorapatite-fluorellestadite from Rydułtowy

	1	2	3	4	5	6	7	8	9	10	11	12	13	14	15	16	17	GM
B <sup>1</sup>	41	57	62	46	<b>106</b>	37	38	49	44	bdl <sup>2</sup>	bdl	bdl	47	54	49	50	36	49
Na	234	178	bdl	264	<b>379</b>	258	258	bdl	bdl	bdl	bdl	248	229	243	bdl	bdl	bdl	249
Mg	241	2439	1300	418	<b>6215</b>	<b>3812</b>	1000	390	160	177	54	60	164	287	306	282	185	404
V	15	17	19	11	21	12	13	17	20	15	bdl	bdl	bdl	17	<b>23</b>	18	17	16
Fe	bdl	bdl	bdl	bdl	bdl	bdl	bdl	bdl	bdl	bdl	bdl	200	<b>684</b>	209	bdl	231	bdl	(285)
Ge	<b>37</b>	bdl	31	bdl	34	bdl	bdl	bdl	bdl	bdl	bdl	bdl	bdl	33	bdl	36	33	(34)
As	112	108	110	73	120	81	94	100	116	<b>128</b>	bdl	bdl	bdl	106	115	108	120	105
Sr	497	592	622	1760	631	2201	1293	802	681	690	2473	3502	<b>6592</b>	601	931	657	707	1072
Y	<b>72</b>	54	60	62	46	32	36	34	35	49	4.4	13	58	52	47	51	35	38
Ba	bdl	bdl	4.6	7.5	9.2	21	10	7.3	4.6	1.9	12	6.2	<b>25</b>	7.8	2.1	7.1	7.8	8.4
La	<b>45</b>	33	33	33	29	19	22	18	20	32	1.7	2.3	11	26	22	28	20	18
Ce	42	46	52	<b>56</b>	38	27	34	31	30	40	3.7	4.1	19	47	38	46	32	29
Pr	17	11	13	12	9.4	6.4	7.0	7.1	7.5	11	0.57	0.50	2.8	9.6	7.9	10	6.8	6.2
Nd	<b>89</b>	63	62	61	52	31	42	37	37	53	2.5	2.4	14	47	39	51	34	31
Sm	<b>23</b>	17	19	14	15	8.7	10	8.7	9.7	14	bdl	bdl	4.2	14	12	15	9.8	12
Eu	<b>5.5</b>	4.0	3.9	3.2	3.4	2.1	2.2	1.9	2.4	3.2	bdl	bdl	0.81	2.4	2.3	3.1	2.0	2.6
Gd	<b>25</b>	19	17	15	14	9.2	12	10	12	17	bdl	bdl	4.4	14	14	16	11	13
Tb	<b>2.7</b>	1.7	1.8	1.7	1.3	0.91	1.1	1.0	1.2	1.4	bdl	bdl	0.61	1.5	1.5	1.5	1.1	1.3
Dy	<b>11</b>	7.3	9.4	8.6	7.1	4.1	5.2	4.0	4.7	7.3	bdl	0.63	4.3	6.3	6.6	7.4	4.9	5.4
Ho	<b>1.5</b>	1.3	1.4	<b>1.5</b>	1.0	0.71	0.80	0.82	0.87	1.0	bdl	bdl	0.86	1.3	1.2	1.3	0.64	1.0
Er	2.9	2.7	3.3	3.2	2.2	1.3	1.8	1.6	1.5	2.7	0.53	0.66	<b>3.4</b>	1.9	2.2	2.5	1.4	1.9
Tm	0.33	bdl	0.22	0.34	bdl	bdl	bdl	bdl	bdl	0.21	bdl	bdl	<b>0.41</b>	0.23	0.24	bdl	bdl	(0.28)
Yb	0.92	1.1	1.2	1.4	0.88	0.61	0.58	0.59	0.66	1.1	0.67	1.7	<b>1.9</b>	1.1	1.2	0.84	bdl	1.0
Lu	bdl	bdl	bdl	bdl	bdl	bdl	bdl	bdl	bdl	bdl	bdl	0.30	0.33	bdl	bdl	bdl	bdl	
W	bdl	bdl	bdl	bdl	bdl	bdl	bdl	bdl	bdl	2.1	1.3	bdl	bdl	bdl	bdl	bdl	bdl	
Pb	bdl	bdl	bdl	bdl	0.62	0.54	bdl	bdl	bdl	bdl	bdl	<b>1.1</b>	0.75	bdl	bdl	bdl	bdl	
Th	<b>3.3</b>	2.4	2.5	1.6	1.7	1.2	1.4	1.2	1.3	1.3	bdl	bdl	bdl	2.0	0.92	1.7	1.1	1.6
U	bdl	0.49	0.30	0.33	bdl	0.40	0.59	0.30	bdl	bdl	bdl	1.3	0.86	<b>1.6</b>	1.2	bdl	bdl	(0.61)

GM – geometric mean; maximum levels are given in bold; <sup>1</sup> Li, Be, Al, K, Sc, Ti, Cr, Mn, Co, Ni, Cu, Zn, Rb, Zr, Nb, Sn, Hf and Ta were below their detection limits; <sup>2</sup> below detection limit

Table 4

Shapiro-Wilk normality test, LDS15 sample

	Li	B	Na	Mg	Al	K	Sc	Ti	V	Cr	Mn	Fe	Cu	Zn	Ge	As	Sr	Y	Zr	Nb
S-W	<b>0.94</b>	0.91	0.80	0.88	0.65	0.83	<b>0.96</b>	0.80	0.88	<b>0.97</b>	<b>0.96</b>	<b>0.94</b>	0.88	0.88	0.77	0.79	0.80	<b>0.96</b>	0.82	0.85
p-value	0.09	<b>0.02</b>	<b>0.0001</b>	<b>0.004</b>	<b>4·10<sup>-7</sup></b>	<b>0.0003</b>	0.64	<b>0.0001</b>	<b>0.004</b>	0.54	0.38	0.11	<b>0.003</b>	<b>0.04</b>	<b>2·10<sup>-5</sup></b>	<b>0.0001</b>	<b>0.0001</b>	0.25	<b>0.0002</b>	<b>0.001</b>
	Ba	La	Ce	Pr	Nd	Sm	Eu	Gd	Tb	Dy	Ho	Er	Tm	Yb	Lu	W	Pb	Th	U	
S-W	0.89	0.81	<b>0.97</b>	<b>0.93</b>	0.89	0.92	<b>0.94</b>	<b>0.96</b>	<b>0.95</b>	<b>0.94</b>	<b>0.95</b>	<b>0.95</b>	<b>0.94</b>	<b>0.93</b>	<b>0.97</b>	0.89	0.82	0.76	0.87	
p-value	<b>0.01</b>	<b>0.0001</b>	0.45	<b>0.04</b>	<b>0.005</b>	<b>0.04</b>	0.10	0.39	0.23	0.11	0.19	0.23	0.09	0.06	0.61	<b>0.01</b>	<b>0.0002</b>	<b>2·10<sup>-3</sup></b>	<b>0.01</b>	

Records with normal distribution and/or with 0.05 are given in bold



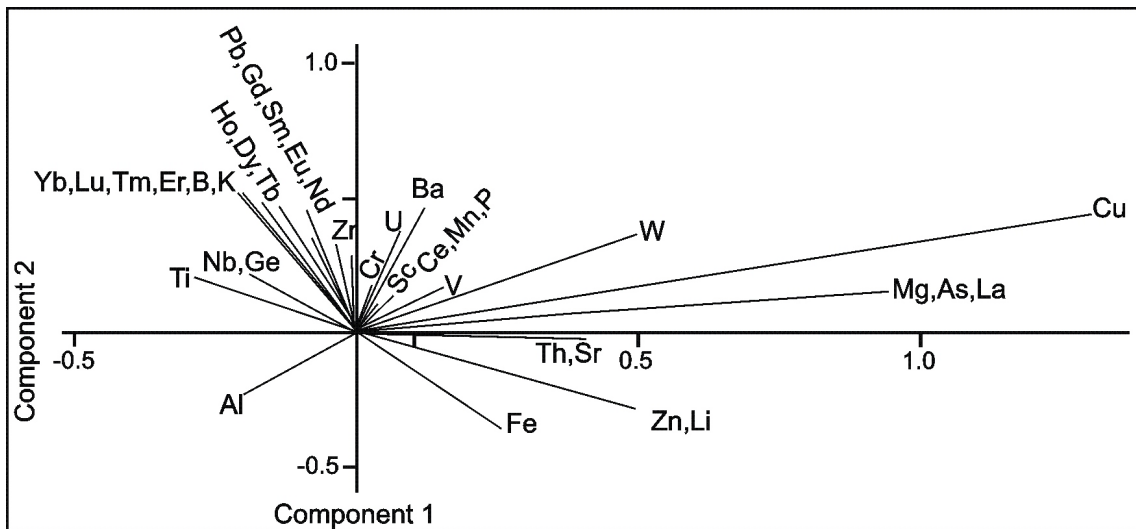


Fig. 3. Principal Component Analysis (PCA) graphical results with element-related eigenvectors, for the LdS15 fluorellestadite; PAST software (Hammer et al., 2001) applied

dysprosium. Least variable elements are arsenic, sodium, vanadium; boron; thulium and holmium. Both normal distribution and 0.05 in the Shapiro-Wilk test (Table 6) is exclusively observed for tungsten. A normal distribution is shown by sodium, magnesium, germanium, arsenic, barium, samarium, europium, gadolinium, terbium, holmium, thulium, ytterbium, thorium and uranium.

The positive Kendall correlations (Table 7), with 0.05 are:

- 0.90: La-Pr, La-Nd, Pr-Nd;
- 0.75 < 0.90: La-Ce to La-Tm, La-Th, Ce-Pr, Ce-Tb, Pr-Sm to Pr-Ho, Nd-Sm, Nd-Eu to Nd-Dy, Sm-Eu to Sm-Dy, Eu-Gd, Gd-Tb to Tb-Ho;
- 0.50 < 0.75: B-Ho, V-As, Y-La, Y-Ce to Y-Er, Ba-Tm, Ce-Nd, Ce-Sm to Ce-Er, Pr-Er, Pr-Th, Nd-Ho, Nd-Er, Nd-Th, Sm-Tb, Sm-Ho, Sm-Th, Eu to Eu-Ho, Gd-Ho, Gd-Er, Gd-Th, Tb-Dy, Dy-Ho, Dy-Er, Dy-Th, Ho-Tm, Ho-Th, Er-Th;
- 0.30 < 0.50: B-V, B-Th, As-Sm to As-Gd, Y-Sm, Y-Gd, Y-Tb, Y-Th, Ce-Mg, Sm-Er, Eu-Er, Tb-Er, Er-Yb, Ce-Th, Eu-Th, Yb-Ho, Yb-Er;

Other relatively strong positive correlations ( $\geq 0.30$ ,  $>0.05$ ) are: B-As, B-La to B-Nd, B-Eu to B-Tb, B-Er, Na-Mg, Mg-La, Mg-Ce, Sr-U, Y-Eu, Tb-Yb, Ho-Yb, Er-Tm and Yb-Tm.

The negative Kendall correlations, with 0.05, are:

- 0.50 < 0.75 Na-Th, Nd-Sr, Gd-Sr;
- 0.30 < 0.50: Ba-Pr, Ba-Gd, Ba-Tb, La-Sr, Pr-Sr, Sm-Sr, Eu-Sr, Tb-Sr, Dy-Sr.

Other relatively strong negative correlations ( $\geq 0.30$ ,  $>0.05$ ) are: B-Na, Na-Y, Na-Tb, Na-Ho to Na-Yb, Mg-As, Mg-U, As-Sr, As-Ba, As-Tm, Sr-Y, Sr-La, Sr-Pr to Sr-Dy, Ba-La, Ba-Nd to Ba-Eu, Ba-Th and Sm-Tm.

The PCA corroborates most of the relations observed above (Fig. 5). Variation is similar in the case of La, Nd, Ce, Pr, Y, Dy, Er, Th and V (~isolinear vectors) and these elements show inversely proportional behaviour towards Sr. Indeed, vertices of the corresponding vectors are very distant. A further positively correlated group is Tb-Gd-Sm-Eu-Ho, that shows inverse-proportional behaviour towards Tm and Ba-Na. The last isolinear vector group concerns B and Mg, inversely correlated with Yb, Sr, and with Ba showing an evident negative correlation with Mg.

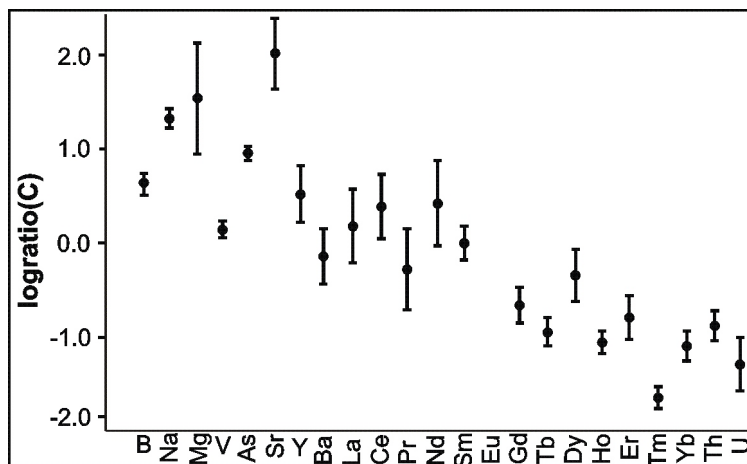


Fig. 4. Mean-and-whisker diagram of element-compositional data variation, the RDTb16c post-coal fluorellestadite; PAST software (Hammer et al., 2001) applied

Table 6

Shapiro-Wilk normality test, RDTb16c sample

	B	Na	Mg	V	Fe	Ge	As	Sr	Y	Ba	La	Ce	Pr
S-W	0.84	<b>0.88</b>	<b>0.93</b>	0.51	0.76	<b>0.91</b>	<b>0.88</b>	0.84	0.71	<b>0.93</b>	0.72	0.69	0.71
p-value	<b>0.02</b>	0.18	0.23	<b>3·10<sup>-6</sup></b>	<b>0.04</b>	0.41	0.06	<b>0.0001</b>	<b>0.0001</b>	<b>0.05</b>	<b>0.0002</b>	<b>0.0001</b>	<b>0.0002</b>
	Nd	Sm	Eu	Gd	Tb	Dy	Ho	Er	Tm	Yb	W	Th	U
S-W	0.71	<b>0.93</b>	<b>0.91</b>	<b>0.90</b>	<b>0.97</b>	0.72	<b>0.94</b>	<b>0.88</b>	<b>0.89</b>	<b>0.95</b>	<b>0.86</b>	<b>0.96</b>	<b>0.90</b>
p-value	<b>0.0002</b>	0.25	0.14	0.09	0.88	<b>0.0003</b>	0.36	<b>0.03</b>	0.29	0.55	<b>0.05</b>	0.68	0.20

Records with normal distribution and/or with 0.05 are given in bold

Table 7

Kendall tau correlation statistics, RDTb16c sample

	B	Na	Mg	V	Ba	La	Ce	Pr	Nd	Sm	Eu	Gd	Tb	Dy	Ho	Er	Tm	Th	U
B	.33																		
Na	.33	.46	.39																
Mg	.40	.47	.32																
V	.46	.47	<b>.60</b>																
As	.39		.32	.32	.40														
Sr			.32	.32	.32	.48	.30	.47	.50	.46	.47	.51	.40	.40					.36
Y	.37		.32			.62	.65	.61	.56	.41	.36	.46	.62	.59	.60	.68			.45
Ba			.40			.32			.34	.38	.39	.47	.41						.31
La	.33	.34		.40	.32	.78	.90	.95	.84	.87	.89	.80	.86	.86	.65				.60
Ce	.38	.39		.65	.72	.77	.72	.65	.65	.56	.65	.65	.76	.73	.67				.42
Pr	.37			.61	.40	.90	.77	.91	.79	.80	.84	.84	.86	.84	.75				.47
Nd	.37	.36		.56	.34	.95	.72	.91	.83	.85	.87	.87	.76	.81	.63				.61
Sm	.40			.46	.41	.84	.65	.79	.83	.83	.87	.87	.74	.78	.57				.69
Eu	.38			.30	.39	.87	.56	.80	.85	.83	.82	.82	.71	.71	.58				.63
Gd	.32			.30	.47	.89	.65	.84	.87	.87	.82	.77	.77	.81	.60				.57
Tb	.31	.33		.40	.62	.80	.76	.86	.76	.74	.71	.77	.74	.74	.76				.36
Dy				.40	.59	.86	.73	.84	.81	.78	.71	.81	.74	.69	.69				.51
Ho	.50	.49		.60	.60	.65	.67	.75	.63	.57	.58	.60	.76	.69	.46				.54
Er	.38	.47		.68		.67	.59	.67	.65	.47	.44	.56	.47	.69	.55				.41
Tm	.60	<b>1</b>			.73				.43				.36		.43				.39
Yb		.52		.42									.36		.46				.39
Th	.44	.73		.45	.31	.60	.47	.61	.67	.69	.63	.57	.60	.51	.54	.51			
U			.42	.36															

Negative values are given in italics; values <0.30 are not shown; these 0.50 and <-0.50 are given in bold; these with 0.05 are underlined

In the PCA graph, the Sr vector is the longest, but it also lacks relation to both PC1 and PC2 due to its relative angle of 45°. In terms of length, it is followed by the collinear Y-LREE-MREE-Er-Mg vector and the Ba vector. Thus, variation of Sr, Ba, most REEs, and Mg is most meaningful. In contrast to that, the shortest vectors are formed by Yb, V, Eu and Th, suggesting their variation is probably unrelated to the PC. The Sr and Ba vectors have their apices (*i*) most distant from that of the REE-Mg vector. Thus, a strong negative correlation of both Sr and Ba with REE-Mg is suggested. Considering the inclination of their vectors to the PC1 axis, W, Eu and Th variability is most dependent on PC1, and that of V on PC2. An evident inverse correlation of Eu and U is observed.

The PCA variance is compared in Table 8. Identical percentage of the variance is found towards the PC1 component. The PC2 component is much less significant in terms of the elemental variance, although it is more meaningful in the case of the RDT analyses.

Anhydrite, closely associated with the French fluorapatite-fluorellestadite, was also studied for comparison. It was shown to be an important carrier of Sr, Mo, and W (Table 9). These admixtures are related to substitution of the celestite, powellite and scheelite end-member equivalents. Substitution of Mo in the LdS anhydrite had been earlier suspected; indeed, Kruszewski et al. (2018a) reported a maximum of 1.74 wt.% MoO<sub>3</sub> in this material.

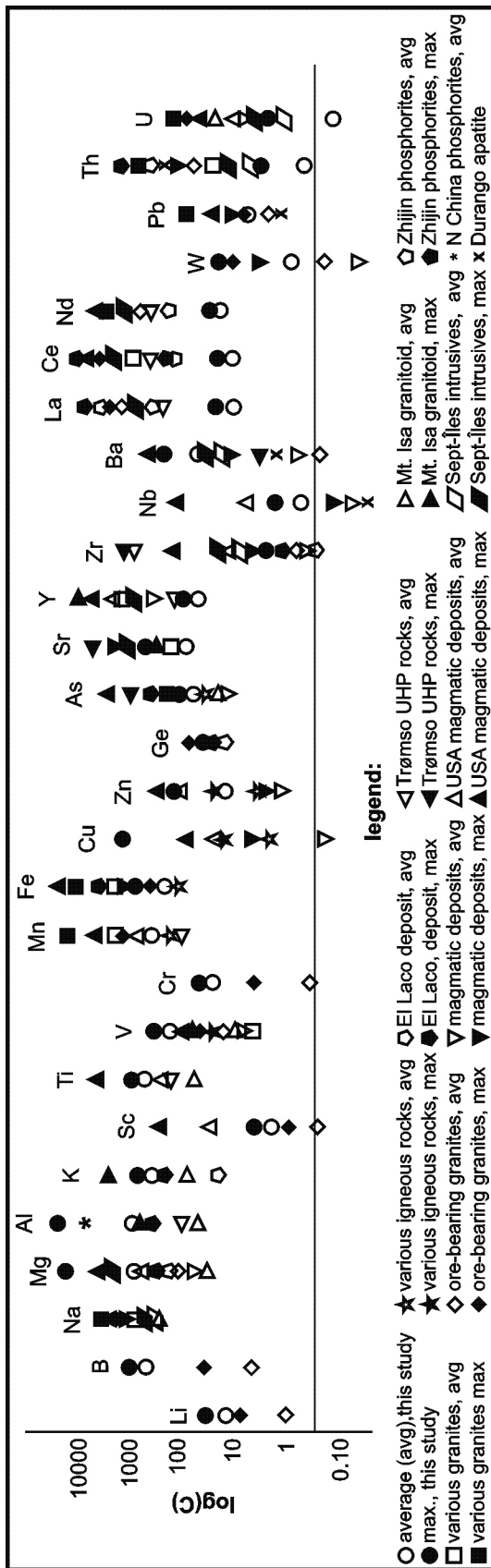


Fig. 5. Principal Component Analysis (PCA) graphical results with element-related eigenvectors, for the RDTb16c fluorellestadite, PAST software (Hammer et al., 2001) applied

Table 8

PCA variance for the LDS and RDTb16c fluorellestadite samples

		Eigenvalue	% variance
LDS15	PC1	0.85	44
	PC2	0.35	18
	PC3	0.17	9
RDTb16c	PC1	0.54	44
	PC2	0.33	27
	PC3	0.11	9

## DISCUSSION

Both the oil-shale (French) and coal-related (Polish) fluorellestadites studied show enrichment in many elements. Boron and germanium are here of a special interest due to scarce published data and being part of the critical elements list. The LdS15 sample seems to be more enriched, although this may also reflect the larger size of the crystals analyzed. Average and maximum TE contents of the French fluorellestadite were compared with published data, including of various igneous rocks, both extrusive and intrusive, and metasomatic rocks, UHP rocks, phosphorites and the Durango apatite standard (Fig. 6). For Li, B, Mg, Al, Cr and Cu, the highest levels measured are simultaneously the maximum contents within this literature-based comparison. Elements for which both the maximum and average contents are higher than in ore-bearing granites include Li, B, Mg, Al, K, Sc, V, Cr, Ge, Zr and Ba. The opposite dependence is observed for the REEs, U, and to some extent also W and Pb. Higher values of K and Y are known for some granitoid-derived (e.g., from Mt. Isa, Queensland, Australia) apatites. In the case of Sc, Fe, Nb, Nd, U and in particular also Ti, Zn, Ba and Pb, enrichment was recorded in some USA magmatic apatite-bearing deposits. The Trømso UHP-lithology apatites also bear more prominent Zr and REE anomalies. The average Mn content of our sample is relatively low, too, being exceeded in apatites from various granites and igneous ore deposits.

Only some of the elements studied show high enrichment compared to average Earth's crust (EC) levels (as listed by Parker, 1967). These include boron, with enrichment factor (EF, calculated as quotient of the measured value versus the average EC value) being as high as 70 for LdS. In the LdS fluorellestadite, the EF for Ge is 10, and that for As is 23. Values for Tm, Y and Dy are >1.5, while those for V, Er, Yb, Eu, Gd and Ho are in the 1-1.4 range. Boron enrichment in the RDT sample is smaller, with the corresponding EF of 7, and the values for Ge being 11, for As 41, for Sr 3, for Eu 2.4, for Gd 2, for Dy 1.2 and for Y 1.1.

REE spider diagrams are shown in Figure 7. These were constructed to illustrate the evident Nd anomaly and its dominance over other REEs in both samples. Clear positive anomalies are also found for Gd, Dy, Er, and Yb for the LdS15 sample, being less prominent in the RDT one. Some Dy anomalies in the LdS fluorellestadite may be slightly larger than Gd anomalies. The positive Ce anomaly only concerns some of the LdS

Average concentrations trace elements (ppm) in anhydrite associated with fluorapatite-fluorellestadite from Lapanouse-de-Sévérac

	1	2	3	4	5	6	7	8	9	10	GM
Li <sup>1</sup>	bdl	2.1	bdl	bdl	bdl	bdl	bdl	2.1	bdl	<b>2.6</b>	
Fe	1575	bdl	bdl	bdl	bdl	bdl	bdl	bdl	bdl	bdl	
Sr	264	<b>329</b>	254	265	265	232	269	249	268	265	265
Mo	inc	4.9	8.1	7.8	<b>11</b>	2.7	4.7	6.7	8.4	4.9	6.3
Ba	115	42	105	86	<b>121</b>	41	56	53	66	48	68
W	inc	bdl	0.57	0.51	0.86	bdl	bdl	bdl	0.61	bdl	

<sup>1</sup> all the other (see Tables 2 and 3) elements measured were below detection limits; bdl – below detection limit; inc – inclusion (contaminated); GM – geometric mean; maximum levels are given in bold

data, while being evident for most of the RDT datapoints. Although the apatite-type structure prefers the Ce<sup>3+</sup> ion due to its larger ionic-size similarity to Ca<sup>2+</sup> (e.g., Terra et al., 2008), the Ce<sup>4+</sup>-Ca<sup>2+</sup> ionic radii difference is 11%, thus being below the diadochy threshold of Goldschmidt. Small positive Ce anomalies in apatites, although not necessarily explained, are known (e.g., Bromiley, 2020).

The PCA results for the LdS15 fluorellestadite allow derivation of some evident trends. Zn, Li, and to some extent also Ti are known to show tetrahedral coordination in minerals (e.g., Berry et al., 2007). A Zn-Li substitution path is known, e.g., in dusmatovite (Sokolova and Pautov, 1995) or zincostauriolite (Chopin et al., 2003). The Al-V diadochy system is also well-documented in mineralogy, although it involves trivalent cations (e.g., Brigatti et al., 2006; Bačík et al., 2018). Separation of Al and V is clearly seen, e.g., in bariandite, Al<sub>0.6</sub>(V<sup>5+</sup>, V<sup>4+</sup>)<sub>8</sub>O<sub>20</sub>·9H<sub>2</sub>O. Al seems to behave differently to both Fe and Ti (non-collinear vectors, with large to moderate intra-vector angles). However, as V in the apatite supergroup is known to occur in its pentavalent state (thus existing in tetrahedral coordination), Al-for-V substitution in the LdS15 fluorapatite-fluorellestadite seems unlikely. A more likely phenomenon is removal of V followed by enrichment in Al, possibly due to changes in the elemental composition of the parent solutions.

Elemental behaviour in the RDT sample fluorellestadite is completely different to that in the LdS sample. Most importantly, B is now clearly correlated with Mg, the BMg pair being inversely correlated with As (in the LdS15 sample B is negatively correlated with Mg). Differences also concern Nd, which in the RDT sample shows correlation with MREE and Pb, and in the LdS15 sample with LREE (including Y). The Dy-HoTb correlation of the French fluorellestadite is not seen in the Polish sample. The Yb-Lu-Tm-Er-B-K correlation of in LdS is also not seen in the RDT sample, where Yb correlates with U. The Pr-Er and Gd-Tb pairs found for the RDT sample cannot be recognised in that from LdS. Scandium also shows different relationships and this is also true of thorium and vanadium. Strontium also shows different correlation, being clearly correlated with Th (LdS) while correlating negatively with the Th-V-Sc-Eu group (RDT). There is a positive correlation of Ge and Nb (isolinear vectors) and Ti. These high-valency elements do not show collinearity with V and W, other high-valency elements, although no clear or strong negative correlation was found either.

#### CRYSTALLOCHEMICAL POSITION OF BORON

Initially, the boron-bearing apatites were thought to exclusively bear the BO<sub>3</sub> (substituting for phosphate) and BO<sub>2</sub> groups; BO<sub>4</sub> groups were not expected (Ito et al., 1988). Both the orthoborate(3–), i.e., BO<sub>3</sub><sup>3–</sup>, and the tetrahedral BO<sub>4</sub><sup>5–</sup>

orthoborate groups were, however, later identified, as shown in Pr<sub>5</sub>(BO<sub>4</sub>)<sub>3-x</sub>(BO<sub>3</sub>)<sub>x</sub>(F,OH)<sub>2.67</sub>O<sub>0.28</sub> (Glätze et al., 2018). The orthoborate anion is also known in so-called condensed apatites, such as Sr<sub>5</sub>(BO<sub>3</sub>)<sub>3</sub>Br (White and ZhiLi, 2003). Boron may also enter hydroxylapatite, to form borohydroxyapatite, nominally Ca<sub>10</sub>{(PO<sub>4</sub>)<sub>6-x</sub>(BO<sub>3</sub>)<sub>x</sub>}{(BO<sub>3</sub>)<sub>y</sub>(BO<sub>2</sub>)<sub>z</sub>(OH)<sub>2-3y-z</sub>} involving a rare charge-compensation process related to the occurrence of square-pyramidal BO<sub>5</sub> units (Ternane et al., 2002). Mazza et al. (2000) excluded the occurrence of planar orthoborate(3–) groups in their La<sub>5</sub>Si<sub>2</sub>BO<sub>13</sub> apatite-type compound, based on displacement factor calculations, and locate B at the T sites.

#### CRYSTALLOCHEMICAL POSITION OF POTASSIUM AND MAGNESIUM

Both potassium and magnesium are known to be involved in apatite biomineralization (e.g., Wiesmann et al., 1998; Serre et al., 1998). Magnesium may be incorporated simultaneously with carbonate ions (Sader et al., 2013). Simpson (1968) synthesized a K-H-substituted apatite at 100°C, with KOH as the source of potassium. His products contain up to 1.7 wt.% K<sub>2</sub>O, with average content reaching 0.97 wt.%. Atomic percentages of K in his materials vary from 0.13 to 0.21 atoms per formula unit (apfu) K, with suggested 0.48–1.24 apfu(H) at the A site, 0.14–0.29 molecules pfu (mpfu) H<sub>4</sub>O<sub>4</sub> at the T site, and 0.84–1.32 mpfu(H<sub>2</sub>O) at the X site. The K-substituted pyrolytical hydroxylapatite of Yokota et al. (2017) contains up to 1.54 mass% K.

#### CRYSTALLOCHEMICAL POSITION OF ALUMINIUM

Magnesioferrite and srebrodolskite – two minerals associated with both the LdS and RDT fluorellestadite – are known sinks of Co (Kruszewski, 2018). This element is usually below the detection limit in the current ICP data. This reflects the quality of the ICP data, where only few inclusion-type records were confirmed. As such, aluminium is most likely present within the structure of the fluorellestadites analysed. Aluminium (LdS sample) negatively correlates with V and W. No positive correlation is observed for the Al-Mg system. Also, Ti is negatively correlated with Zn and Li, and to some extent with Fe, but does not show clear correlation with Mg. The lack of positive Al-Mg, Al-Fe, Mg-Mn and Mn-Fe correlations may exclude the possibility of these four elements being derived from tiny, sub-micron inclusions of both magnesioferrite and srebrodolskite that are otherwise present in the matrix. However, both Al and Ti (but not Mg) may show tetrahedral crystallochemical affinity. This could explain the moderately high positive Al-Ti correlation (r = 0.50).

Kharamova et al. (2015) report the occurrence of tetrahedral AlO<sub>4</sub> anions in aluminium-doped lanthanum silicate-oxide

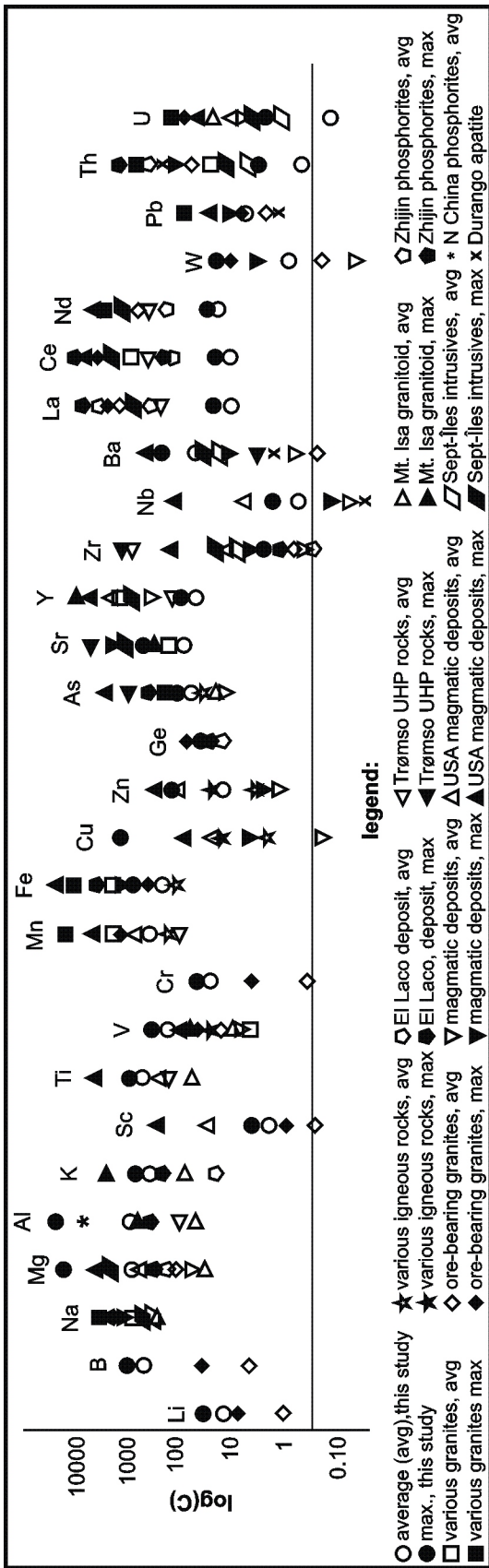


Fig. 6. Comparison of average (geometric mean) and maximum trace element contents in the LdS15 fluorellestadite with published data: various granites (Sha and Chappell, 1999), various igneous rocks (and their ores; Belousova et al., 2002), ore-bearing granites (Duan and Jiang, 2018), El Laco magnetite-apatite deposit (La Cruz et al., 2020), various magmatic (porphyry-included and other) ore deposits (Mao et al., 2016), Ultra-High-Pressure (UHP) carbonate-silicate rocks of the Trømso Nappe, Norway (Broska et al., 2014), various USA ore deposits (Mercer et al., 2016), Mt. Isa granitoids (Belousova et al., 2001), Sept-iles intrusive rocks (Tollari et al., 2018), Zhijin-deposit phosphorites (Xiqiang et al., 2020), North China phosphorites (Guo et al., 2014), and the Durango apatite standard (Kimura et al., 2000)

apatite, nominally  $La_{10-x}(SiO_4)_6O_{3-3x/2}$ . However, they also mention the occurrence of  $AlO_6$  and traces of  $AlO_5$  in polyhedral coordination in this material. Elevated temperature clearly diminishes the content of  $AlO_6$ , with both  $AlO_6$  and  $AlO_5$  lacking at the 800°C stage of calcination of the protolith. Transformation of these units into  $AlO_4$  is said to be complete at  $T > 500^\circ C$ . Kharlamova et al. (2015) stated that the  $AlO_4$  in the apatite-type structure is typically distorted, and the occurrence of this type of polyhedron is corroborated by IR studies.

CRYSTALLOCHEMICAL POSITION OF TITANIUM

Positive values in the Ti-Ge and Ti-As ( $\rho > 0.50$  in both cases) may confirm the occurrence of  $^{IV}Ti$  in the LdS fluorellestadite. However, a much stronger positive correlation concerns the Ti-Nb system. This recalls the Ti-Nb diadochy at the octahedral sites of minerals such as rutile (e.g., Sahasrabudhe et al., 2016) and titano(niobo)silicates (e.g., Rocha et al., 1996). On the other hand, Nb seems to be negatively correlated with As ( $\rho = -0.47$ ) and shows a weak positive correlation with B ( $\rho = 0.31$ ). It is thus rather attributable to the T site of the ASG structural type. Tetrahedral "titanate",  $TiO_4^{4-}$ , is known in a Ti-modified synthetic hydroxylapatite (Adamiano et al., 2017).

CRYSTALLOCHEMICAL POSITION OF OTHER ADMIXING ELEMENTS

Bostick et al. (2003) list the following levels of elemental affinity to the apatite-type structure:

- strong affinity:  $Mn^{2+}$ ,  $Cu^{2+}$ ,  $Cd^{2+}$ ,  $Sb(III)$  (as  $SbO^+$ ),  $Pb^{2+}$ ,  $Hg^{2+}$ ,  $Th$ ,  $U(VI)$  (as  $UO_2^{2+}$ , although with precipitation of the synthetic analogue of autunite);
- modest affinity:  $V(V)$  (as  $VO_4^{3-}$ ),  $Fe^{2+}$ ,  $Zn$ ,  $Ni$ ,  $As(V)$  (as  $AsO_4^{3-}$ ),  $Sr$ ,  $Ba$ ;
- low or lacking affinity:  $Se(IV)$  (as  $SeO_3^{2-}$ ; elevated at  $pH = 8$ ),  $Cr(VI)$  (as  $CrO_4^{2-}$ ),  $Mo(VI)$  (as  $MoO_4^{2-}$ ),  $TcO_4^-$ .

Synthetic chromate apatites are also known, as exemplified by  $Sr_5(CrO_4)_3F$  (Đorđević et al., 2008). The latter compound, however, bears pentavalent chromium, which is not expected to be stable in natural conditions. We rather suspect chromium to follow both As and V, and to be present as tetrahedral chromate(VI) anions in the LdS fluorellestadite. Chromate(VI) minerals, such as chromatite,  $CaCrO_4$ , or the ettringite-group species siwaqaite,  $Ca_6Al_2(CrO_4)_3(OH)_{12} \cdot 26H_2O$ , are known from PM rocks of the well-known Hatrurim Formation and the related Daba-Siwaqa complex (Israel, Jordan, and Palestine sites) that is clearly analogous to a burning heap environment (Gross, 1977; Juroszek et al., 2020).

NEODYMIUM ENRICHMENT

The anomalous Nd behaviour (enrichment) may be explained by its coordination. The  $Nd^{3+}$  ion fits to the  $^{IX}Ca1$  site best of all the REEs (e.g., Fleet and Pan,

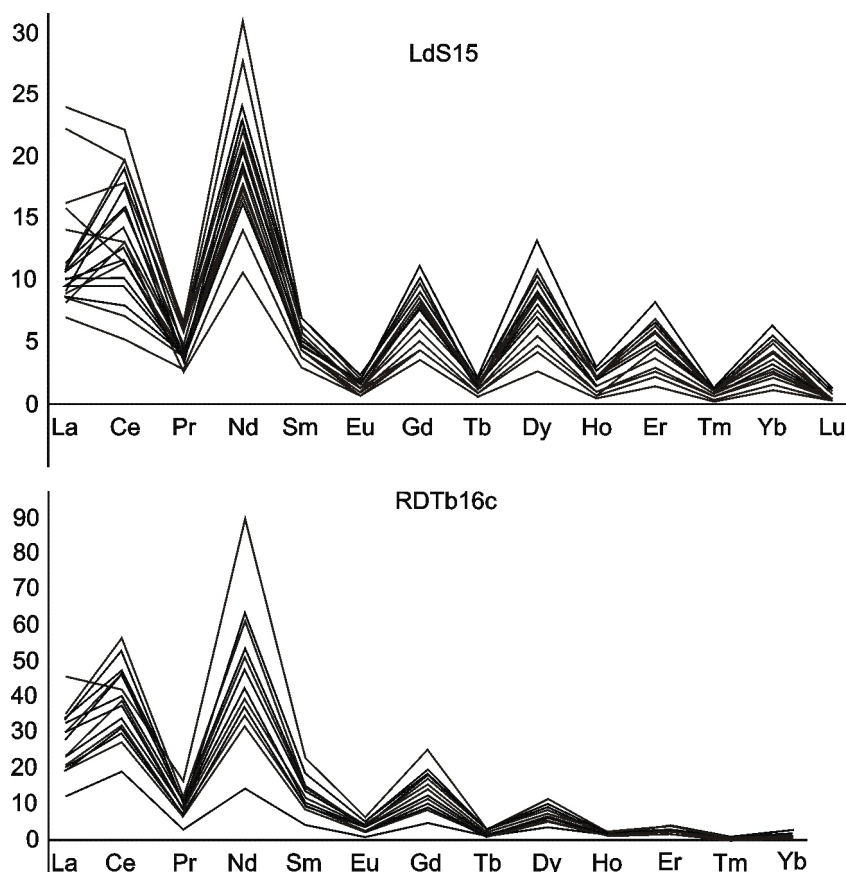


Fig. 7. REE spider diagrams of the two fluorellestadite samples

The diagrams are not chondrite-normalized, to show the clear Nd dominance and anomaly of the material studied

1995). Nd enrichment in apatites seems to be important in terms of the crystallochemistry of other elements, including Na. Indeed, Fleet and Pan (1995) found that sodium prefers the Ca1 site in La- and Gd-dominant analogues, but is found at both the Ca1 and Ca2 sites in the Nd-dominant analogue. Chakhmouradian et al. (2017) noted a non-conform partitioning of the REEs in carbonatitic apatites due to differences in uptake between the LREEs (Ca1 site preference) and HREEs (Ca2 site preference). They also point to a crest between Pr and Nd, and that intermediate-size REEs (Sm-Tb) may be accommodated equally. On the other hand, Fleet and Pan (1995) structurally refined a Nd-substituted fluorapatite using a model where 80 atomic % of Nd is partitioned into the Ca2 site. They also note that in a Nd-rich fluorapatite (but not in La-, Gd-, or Dy-dominant ones) sodium not only enters the Ca1 site, but is also present at the Ca2 site. The observations of Hughes et al. (vide Fleet and Pan, 1995) suggest that while La, Ce and Pr would rather favour the Ca2 site, and Pm and Sm the Ca1 site, Nd would be exceptional in showing affinity to both the Ca sites. This behaviour of Nd would also explain our observations, as with two sites available more Nd would enter the structure than in the case of the remaining REEs.

Further information regarding LREE enrichment/depletion in apatites came from the work of Yakymchuk (2017) who studied apatite behaviour during partial melting of metapelites – a process similar to the one generating fluorellestadite-bearing PM rocks in the current study. Monazite would be the dominant REE sink in such systems. However, apatite, as opposed to monazite, is predicted to withstand ultra-high temperatures.

Thus, the stability of monazite above the solidus is diminished by the presence of LREE-rich apatite.

#### POTENTIAL SOURCES OF THE MOST ENRICHED ELEMENTS

The most potent element source in the coal-waste mining heaps is coal itself. Both boron and germanium are known as coalophile elements, with their Coal Affinity Indices (CAIs) of 47 and 2.4, respectively (Ketrís and Yudovich, 2009), which are higher than average crustal levels (Parker, 1967). The same is true for arsenic (CAI = 9.0), bismuth, mercury, molybdenum, antimony, selenium and tellurium. Marginal parts of coal deposits are known to be especially Ge-enriched, and extremely Ge-rich coals are exploited in both Russia (Pavlovka deposit) and China (e.g., Wulatunga and Lincang deposits; Seredin and Finkelman, 2008).

At the Lapanouse deposit, the Lower Jurassic black oil shale is interbedded with limestone and intercalated between marls and marly shales (Gatel et al., 2015). Some marls are locally pyritous. A “black lignite” is sporadically found there, too. The mineral composition of the oil shale comprises calcite-gypsum intergrowths, quartz, pyrite, microcline, “illite”, and chlorite. No geochemical data for the local rocks could be found. Lapidus et al. (2022) state that the Ge content of oil shales is, generally, lower than that of coals. However, they list deposits where the content may reach 14 (Negev, Israel) or even 50 (Novodmitrovsk, Ukraine) ppm. Some shales of this kind may bear as much as 20 ppm Be (Boysun, Tajikistan), ~1000 ppm Sr (Kashpir, Russia, with just slightly less in Negev), >1000 ppm

Mo (Boysun; Suzak, Uzbekistan), 30 ppm Ga (Boysun, Suzak), 2900 ppm V (Boysun) and 100 ppm La (Suzak). Background concentrations of As in such shales may also be quite high at 30 ppm. Considering the crystallochemistry of the slag-forming minerals at Lapanouse (Kruszewski et al., 2018), the sedimentary protolith must have been enriched especially in Cr (based on enrichment in spinels, clinopyroxenes, cuspidine, hematite, perovskite, fluorellestadite and even titanite), V (considering the occurrence of pliniusite and enrichment in perovskite, hematite-pseudobrookite solid solution, and titanite), Mo (based on the occurrence of the powellite-equivalent end-member in anhydrite), Ba (based on enrichment in feldspars and leucite, and the occurrence of “Ba-petalite”,  $\text{BaAlSi}_3\text{AlO}_{10}$ ), Sr (considering its enrichment of fluorellestadite, plagioclase, perovskite, and levantite, the last formerly wrongly attributed to “depmeierite-latinumite system”), but also Ni, Zn, and less so Co (somewhat enriched in hematite, pseudobrookite-hematite solid solution, and spinels). As such, the most reliable source for the substitutes in the French fluorellestadite is the organic matter of the oil shale.

Boron, along with lithium and strontium, is enriched in marine waters (e.g., Brunskill et al., 2003; Zhang et al., 2022). This explains the preferential enrichment of, especially, boron and lithium in shales (e.g., Warner et al., 2014). In the case of the USCB coals, B enrichment is not observed (<20 ppm, own unpublished data). Boron was not measured in any pyrometamorphic mineral of the USCB area. A slightly elevated content of 33 ppm was measured in alunite-cristobalite shales of a heap in Radlin, with a similar value of 29 ppm derived for just a single coaly shale sample. Similar levels were found in three exhalative (gas-vent) deposits. A much higher content of 125 ppm was detected in ammonium-rich gas-condensate sulfate deposits at a heap in Świętochłowice (Kruszewski, unpublished data). Numerous ash-condensate samples from different heaps show B as one of just a few clearly enriched elements, thus confirming B affinity to the coal-fire gas phase. Boron may preferentially enter the structure of mullite (e.g., Romero et al., 2021) – a common component of coal-fire pyrometamorphic minerals – via its gas-phase transfer.

Germanium enrichment in newly-formed minerals in burning and burnt post-coal mining waste heaps in Poland is rarely observed. A prominent exception is a single-sample cuspidine, with its maximum Ge content of 941 ppm, with <300 ppm in a few gehlenite crystals studied (Kruszewski, 2018). This may be due to volatilization of Ge, possibly in the form of  $\text{GeCl}_4$  and some other species, in exhalative vents (Kruszewski et al., 2018b). Ge levels in USCB coals and shales are in the 0.20-0.50 ppm range. The local pyrite shows a 0.30 ppm content (Kruszewski, unpublished data).

Arsenic enrichment in the Rydułtowy apatite-group species as studied by EPMA was found only in a single analysis (0.23 wt.%  $\text{As}_2\text{O}_5$ ; Kruszewski, 2018). Pyrite is a known local As concentrator (e.g., 26 ppm level; Kruszewski, unpublished data). The Rydułtowy coal is As-low at just 0.50 ppm, while some clayey deposits collected at the heap there show 5.3 ppm (Kruszewski, unpublished data). Coaly shales collected at some USCB heaps are also good As sources, with average 8.6 ppm content (Kruszewski, unpublished data).

Strontium is commonly reported in analyses of the pyrometamorphic apatite-group minerals of the USCB area. The average strontium content in the Rydułtowy apatites-ellestadites is 0.14–0.17 wt.% Sr. Much higher contents (8.05 wt.% Sr on average) were detected in a rare celsian-slawnite solid solution within a yellow metapelite from a heap in Jankowice Rybnickie (Kruszewski, 2018). The Rydułtowy coal is relatively rich in Sr, at 235 ppm. This is, however, an exception considering the average 73 ppm in the

USCB coals, and just 30 ppm in the shales (Kruszewski, unpublished data). However, the major Sr concentrator in the USCB heaps is gypsum, with contents peaking at 945, or even 2000 ppm (Kruszewski, 2018). The primary Sr source is expected to be carbonate minerals. Indeed, Parzenty et al. (2020) found a relatively high correlation coefficient for the Sr-carbonate system of the USCB coals. Still, they report a higher  $r^2$  for the Sr- $\text{P}_2\text{O}_5$  system, suggestive of Sr containment in primary apatite-group minerals. The LDS source rocks are rich in gypsum (a potential Sr source; 8% in the modal composition of the oil shale; Gatel et al., 2014). In the USCB coal deposits, baryte mineralization is known, bearing Sr admixtures (e.g., with 1.6 mol.%  $\text{SrSO}_4$  component in baryte from the “Marcel” mine). Strontian baryte is a common accessory phase of many waste rocks from the USCB BWHs, including metacarbonate slags from Rydułtowy, where celestine is also rarely encountered (Kruszewski, 2018). Although the local apatite-supergroup species are, in general, low in Sr (up to 0.25 wt.% SrO), Sr is also found in other local minerals (e.g., bassanite, fluorite).

#### STATISTICS – DISCUSSION

The high input of the PC1 component in the PCA, identical for both the samples studied, suggests the prevalence of a single source for the elemental variation. This factor is likely the ionic radii, as shown by collinearity of the vectors attributed to Zn and Li, Nb and Ge (with the Ti vector nearby), and the MREE groups (LDS sample), U+Yb and Y+LREE groups (RDT sample), and the HREE group (in both samples). The vectors in these cases are usually short, suggesting a higher significance of the dependencies listed. On the other hand, the vectors listed form more acute angles with the PC2 component. The latter could be attributed to the elements’ sources. Indeed, the Th+Sr, Mg+As+La vectors, relative to elements with >15% diadochy threshold, form acute angles with PC2. A mixed influence of both the PC components is exemplified by positions of the REEs’ vectors in the RDT case, which are either acutely inclined towards the PC2 component (Ce, Y, Nd, La, Pr, Er, Dy), or towards PC1 (Ho, Tm, Yb, Gd). The different position of the Y and HREE vectors is somewhat unexpected.

The influence of the source factor is possibly exemplified by the Sr-Th pair, for which an opposite behaviour is observed when comparing the two samples studied. In the LDS sample there is a clear positive correlation, suggesting (considering the vectors’ position relative to the PC2 component) a common source. In the RDT sample Sr is clearly negatively correlated with Th; Sr also does not show any positive correlation with any other element. The observed differences in the Th-Sr relation cannot be simply explained by preferential crystallochemical behaviour. According to Terra et al. (2008) strontium prefers the Ca1 site of the apatite-type structure at Sr levels <0.1 apfu – a condition fulfilled by both of our samples. Luo et al. (2009) found Th (and U) strongly preferring the Ca2 site, with  $\text{U}^{4+}$  being almost the exclusive form in F-rich apatite. As such, no large differences in the site preference of Sr and Th are expected in the samples studied.

Juxtaposed ionic (thermochemical) radii sizes of the particular elements known or suspected to occur in natural apatite-type structures are to be found in the Appendix 1. Elements with coinciding ionic (thermochemical) radii are:  $\text{VI}^{\text{K}} - \text{Ba} - \text{IX}^{\text{Pb}}; \text{IX}^{\text{Na}} - \text{IX}^{\text{La}}; \text{VI}^{\text{Pb}} - \text{IX}^{\text{Ce}^{3+}}; \text{VIII}^{\text{Na}} - \text{IX}^{\text{Ca}} - \text{Sr} - \text{VIII}^{\text{La}} - \text{IX}^{\text{Nd}}; \text{VII}^{\text{Na}} - \text{VIII}^{\text{Pr}} - \text{VIII}^{\text{Nd}}; \text{VI}^{\text{Na}} - \text{Sm} - (\text{Eu-Gd-Tb-Dy-Ho}); \text{VI}^{\text{Ca}} - \text{Er-Tm-Yb}; \text{VIII}^{\text{Sc}}; \text{VI}^{\text{Mn}^{2+}} - \text{VI}^{\text{Cu}^{2+}} - \text{VI}^{\text{Zn}} - \text{VI}^{\text{Sc}} - \text{VI}^{\text{Zr}}; \text{IV}^{\text{Mn}^{2+}} - \text{VI}^{\text{Nb}}; \text{IV}^{\text{Li}} - \text{IV}^{\text{Mg}} - \text{IV}^{\text{Cu}^{2+}} - \text{VI}^{\text{Fe}^{2+}} - \text{IV}^{\text{Zn}} - \text{VI}^{\text{Fe}^{3+}} - \text{VI}^{\text{Mn}^{3+}} - \text{VI}^{\text{Ti}^{4+}}; \text{VI}^{\text{Al}} - \text{IV}^{\text{Fe}^{3+}} - \text{IV}^{\text{Nb}}; \text{IV}^{\text{Al}} - \text{Ge}^{4+} - \text{IV}^{\text{Ti}^{4+}} - \text{W}^{6+}; \text{V}^{5+} - \text{As}^{5+} - \text{Mn}^{5+}; \text{Si}^{4+} - \text{Cr}^{6+}; \text{C}^{4+} - \text{P}^{5+};$  and  $\text{IV}^{\text{B}} - \text{S}^{6+}$ . Among anions, three pairs are evident:  $\text{CrO}_4^{2-} -$

$\text{SiO}_4^{4-}$ ;  $\text{AsO}_4^{3-}$  -  $\text{GeO}_4^{4-}$  and  $\text{PO}_4^{3-}$  -  $\text{SO}_4^{2-}$ . Substitutions in the apatites studied follow these dependencies at least in particular. This, however, needs confirmation via single-crystal structure modelling. The substitution of all the listed tetrahedral anions in the minerals studied may be due to common sources, i.e., organic matter (Lapanouse), and organic matter plus pyrite (Rydułtowy), as noted in the Section 4.7.

## CONCLUSIONS

The current study has shown that ASG minerals of fossil fuel-fire zones may represent important and rich carriers of numerous TEs. This includes germanium – one of the critical raw materials recognized by the EU. In terms of both TE content and occurrence confirmed in both of the samples studied, this

enrichment ( $>50$  ppm on average) is especially true for aluminium, magnesium, sodium, iron, strontium, boron and arsenic. Highly elevated amounts of K and Ti were also found for the LdS sample. An essential finding is germanium enrichment, seen in both samples. Application of the LAICPMS method seems to exclude the possibility that the Al and Mg are contained in mineral inclusions in the ASG individuals. Rather, they are part of the ASG structure. Further studies on a larger sample set, including Single-Crystal X-Ray Diffraction and Nuclear Magnetic Resonance (for B, Al, and possibly Ge), are planned to test these conclusions.

**Acknowledgements.** This paper was funded by the statutory funds of the Ministry of Higher Education and Science, Poland, for the year 2019.

## REFERENCES

- Adamiano, A., Sangiorgi, N., Sprio, S., Ruffini, A., Sandri, M., Sanson, A., Gras, P., Grossin, D., Francès, C., Chatzipanagis, K., Bilton, M., Marzec, B., Varesano, A., Meldrum, F., Kröger, R., Tampieri, A., 2017. Biomineraliation of a titanium-modified hydroxyapatite semiconductor on conductive wool fibers. *Journal of Materials Chemistry B*, **5**: 7608–7621; <https://doi.org/10.1039/C7TB00211D>
- Azadbakht, Z., Lentz, D.R., McFarlane, C.R.M., 2018. Apatite chemical compositions from Acadian-related granitoids of New Brunswick, Canada: implications for petrogenesis and metallogenesis. *Minerals*, **8**: 598; <https://doi.org/10.3390/min8120598>
- Bačík, P., Uher, P., Kozáková, P., Števkó, M., Ozdín, D., Vaculovic, T., 2018. Vanadian and chromian garnet- and epidote-supergroup minerals in metamorphosed Paleozoic black shales from Čierna Lehota, Strážovské vrchy Mts., Slovakia: crystal chemistry and evolution. *Mineralogical Magazine*, **82**: 889–911; <https://doi.org/10.1180/minmag.2017.081.068>
- Bech, J., Reverter, F., Tume, P., Sánchez, P., Delgado, R., Suarez, M., Lansac, A., Roca, N., 2010. Trace elements in phosphorites of different provenance. 19<sup>th</sup> World Congress of Soil Sciences, Soil Solutions for a Changing World, 1–6 August 2010, Brisbane, Australia: 120–122.
- Belousova, E.A., Walters, S., Griffin, W.L., O'Reilly, S.Y., 2001. Trace-element signatures of apatites in granitoids from the Mt Isa Inlier, northwestern Queensland. *Australian Journal of Earth Sciences*, **48**: 603–619; <https://doi.org/10.1046/j.1440-0952.2001.00879.x>
- Belousova, E.A., Grittin, W.L., O'Reilly, S.Y., Fisher, N.I., 2002. Apatite as an indicator mineral for mineral exploration: trace-element compositions and their relationship to host rock type. *Journal of Geochemical Exploration*, **76**: 45–69; [https://doi.org/10.1016/S0375-6742\(02\)00204-2](https://doi.org/10.1016/S0375-6742(02)00204-2)
- Berry, A.J., Walker, A.M., Hermann, J., O'Neil, H., Foran, G.J., Gale, J.D., 2007. Titanium substitution mechanisms in forsterite. *Chemical Geology*, **242**: 176–186; <https://doi.org/10.1016/j.chemgeo.2007.03.010>
- Bishady, A.M., Farag, N.M., Mira, H.I., El-Sawey, E.-S.H., Negm, S.H., 2019. A contribution to the geochemistry of El-Sibaiya phosphorites, Nile Valley. *Nuclear Sciences Scientific Journal*, **8**: 39–58; <https://doi.org/10.21608/nssj.2019.29945>
- Blengini, G.A., Mathieux, F., Mancini, L., Nyberg, M., Viegas, H.M. (eds.); Salminen, J., Garbarino, E., Orveillon, G., Saveryn, H., Mateos Aquilino, V., Llorens González, T., García Polonio, F., Horckmans, L., D'Hugues, P., Balomenos, E., Dino, G., de la Feld, M., Mádaí, F., Földessy, J., Mucsi, G., Gombkötő, I., Calleja, I., 2019. Recovery of critical and other raw materials from mining waste and landfills: State of play on existing practices. *JCR Science for Policy Report*, EUR 29744 EN, Publications Office of the European Union, Luxembourg, ISBN 978-92-76-03391-2; <https://doi.org/10.2760/494020>, JRC116131; <https://doi.org/10.2760/600775>
- Bostick, W.D., Stevenson, R.J., Harris, L.A., Perry, D., Hall, J.R., Shoemaker, J.L., Jarabek, R.J., Munday, E.B., 2003. Use of apatite for chemical stabilization of subsurface contaminants. Final Report. U.S. Department of Energy, National Energy Technology Laboratory; <https://doi.org/10.2172/820754>
- Bowles, J.F.W., Cook, N.J., Sundblad, K., Jonsson, E., Deady, E., Hughes, H.S.R., 2018. Critical-metal mineralogy and ore genesis: contributions from the European Mineralogical Conference held in Rimini, September 2016. *Mineralogical Magazine*, **82** (S1): S1–S4; <https://doi.org/10.1180/minmag.2017.081.110>
- Brigatti, M.F., Caprilli, E., Marchesini, M., 2006. Poppiite, the  $\text{V}^{3+}$  end-member of the pumpellyite group: description and crystal structure. *American Mineralogist*, **91**: 584–588; <https://doi.org/10.2138/am.2006.2033>
- Bromiley, G.D., 2020. Do concentrations of Mn, Eu and Ce in apatite reliably record oxygen fugacity in magmas? *Lithos*, **384–385**: 105900; [doi.org/10.1016/j.lithos.2020.105900](https://doi.org/10.1016/j.lithos.2020.105900)
- Broska, I., Krogh Ravna, E.J., Vojtko, P., Janák, M., Konečný, P., Pentrák, M., Bačík, P., Luptáková, J., Kullerud, K., 2014. Oriented inclusion in apatite in a post-UHP fluid-mediated regime (Tromsø Nappe, Norway). *European Journal of Mineralogy*, **26**: 623–634; <https://doi.org/10.1127/0935-1221/2014/0026-2396>
- Brounce, M., Boyce, J., McCubbin, F.M., Humphreys, J., Reppart, J., Stolper, E., Eiler, J., 2019. The oxidation state of sulfur in lunar apatite. *American Mineralogist*, **104**: 307–312; <https://doi.org/10.2138/am-2019-6804>
- Brunskill, G.J., Zagorskis, I., Pfitzner, J., 2003. Geochemical mass balance for lithium, boron, and strontium in the Gulf of Papua, Papua New Guinea (project TROPICS). *Geochimica et Cosmochimica Acta*, **67**: 3365–3383; [https://doi.org/10.1016/S0016-7037\(02\)01410-2](https://doi.org/10.1016/S0016-7037(02)01410-2)
- Chakhmouradian, A.R., Reguir, E.P., Zaitsev, A.N., Couëslan, C., Xu, C., Kynický, J., Mumin, H., Yang, P., 2017. Apatite in carbonatitic rocks: Compositional variation, zoning, element partitioning and petrogenetic significance. *Lithos*, **274–275**: 188–213; <https://doi.org/10.1016/j.lithos.2016.12.037>
- Ciesielczuk, J., Kruszewski, Ł., Majka, J., 2015. Comparative mineralogical study of thermally-altered coal-dump waste, natural rocks and the products of laboratory heating experiments. *International Journal of Coal Geology*, **139**: 114–141; <https://doi.org/10.1016/j.coal.2014.08.013>
- Chopin, C., Goffé, B., Ungaretti, L., Oberti, R., 2003. Magnesio-staurrolite and zincostaurrolite: mineral description with a petrogenetic and crystal-chemical update. *European Journal*

- of Mineralogy, **15**: 167–176; <https://doi.org/10.1127/0935-1221/2003/0001-0167>
- Dong, P., 2009.** Halogen-element (F, Cl, and Br) behaviour in apatites, scapolite, and sodalite: an experimental investigation with field applications. Ph.D. thesis, College of Graduate Studies and Research, Department of Geological Sciences, University of Saskatchewan, Saskatoon.
- Duan, D.-F., Jiang, S.-Y., 2018.** Major, trace and rare earth elements of apatite and zircon U-Pb ages of ore-associated and barren granitoids from the Edong ore district, South China. Data in Brief, **20**: 1587–1601; <https://doi.org/10.1016/j.dib.2018.08.154>.
- Đorđević, T., Šutović, S., Stojanović, J., Karanović, L., 2008.** Sr, Ba and Cd arsenates with the apatite-type structure. Acta Crystallographica C, **64**: i82–i86; <https://doi.org/10.1107/S0108270108023457>.
- European Commission, 2017.** Communication from the Commission to the European Parliament, the Council, the European Economic and Social Committee and the Committee of the Regions on the 2017 list of Critical Raw Materials for the EU. Brussels, 13.9.2017, COM(2017) 490 final; <https://eur-lex.europa.eu/>
- Fleet, M.E., Liu, X., 2007.** Coupled substitution of type A and B carbonate in sodium-bearing apatite. Biomaterials, **28**: 916–926; <https://doi.org/10.1016/j.biomaterials.2006.11.003>
- Fleet, M.E., Liu, X., 2008.** Accommodation of the carbonate ion in fluorapatite synthesized at high pressure. American Mineralogist, **93**: 1460–1469; <https://doi.org/10.2138/am.2008.2786>
- Fleet, M.E., Pan, Y., 1995.** Site preference of rare earth elements in fluorapatite. American Mineralogist, **80**: 329–335; <https://doi.org/10.2138/am-1995-3-414>
- Glätze, M., Pitscheider, A., Oeckler, O., Wurst, K., Huppertz, H., 2018.** A high-pressure praseodymium fluoride borate linking multiple structural features of apatite-type compounds. Chemistry – A European Journal, **25**: 1767–1772; <https://doi.org/10.1002/chem.201805092>.
- Gross, S., 1977.** The mineralogy of the Hatrurim Formation, Israel. Geological Survey of Israel, **70**: 1–80.
- Guo, Q., Liao, L., Xia, Z., Liu, H., 2014.** Composition determination and cathodoluminescence of natural apatite from different phosphate deposits in Northern China. JOM, **66**: 992–997; <https://doi.org/10.1007/s11837-014-0955-6>.
- Hammer, O., Harper, D.A.T., Ryan, P.D., 2001.** PAST: Paleontological Statistics Software Package for Education and Data Analysis. Palaeontologia Electronica, **4**: 1–9.
- Hughes, J.M., Rakovan, J., 2015.** Structurally robust, chemically diverse: apatite and apatite supergroup minerals. Elements, **11**: 165–170; <https://doi.org/10.2113/gselements.11.3.165>
- Ito, A., Aoki, H., Akao, M., Miura, N., Otsuka, R., Tsutsumi, S., 1988.** Structure of borate groups in boron-containing apatite. Journal of the Ceramic Society of Japan, **96**: 707–709; <https://doi.org/10.2109/jcersj.96.709>
- Jenkins, H.D.B., Thakur, K.P., 1979.** Reappraisal of thermochemical radii for complex ions. Journal of Chemical Education, **56**: 576; <https://www.wiredchemist.com/chemistry/data/thermochemical-radii-anions>; <https://doi.org/10.1021/ed056p576>
- Juroszek, R., Krüger, B., Galuskina, I., Krüger, H., Vapnik, Y., Galuskin, E., 2020.** Siwaqaite, Ca<sub>6</sub>Al<sub>2</sub>(CrO<sub>4</sub>)<sub>3</sub>(OH)<sub>12</sub>·26H<sub>2</sub>O, a new mineral of the ettringite group from the pyrometamorphic Daba-Siwaqa complex, Jordan. American Mineralogist, **105**: 409–421; <https://doi.org/10.2138/am-2020-7208>
- Ketris, M.P., Yudovich, Ya.E., 2009.** Estimations of Clarkes for Carbonaceous biolithes: world averages for trace element contents in black shales and coals. International Journal of Coal Geology, **78**: 135–148; <https://doi.org/10.1016/j.coal.2009.01.002>
- Kharlamova, T., Vodyankina, O., Matveev, A., Stathopoulos, V., Ishchenko, A., Khabibulin, D., Sadykov, V., 2015.** The structure and texture genesis of apatite-type lanthanum silicates during their synthesis by co-precipitation. Ceramics International, **41**: 13393–13408; <https://doi.org/10.1016/j.ceramint.2015.07.128>
- Kimura, J.-I., Danhara, T., Iwano, H., 2000.** A preliminary report on trace element determinations in zircon and apatite crystals using Excimer Laser Ablation-Inductively Coupled Plasma Mass Spectrometry (ExLA-ICPMS). Fission Track News Letter, **13**: 11–20.
- Kruszewski, Ł., 2008.** Apatite-ellestadite solid solution and associated minerals of metacarbonate slags from burning coal dump in Rydułtowy (Upper Silesia). Mineralogia – Special Papers, **32**: 100.
- Kruszewski, Ł., 2018.** Geochemical Behavior of Trace Elements in the Upper and Lower Silesian Basin Coal-Fire Gob Piles of Poland. In: Coal and Peat Fires: A Global Perspective, **5** – “Case Studies – Advances in Field and Laboratory Research” (ed. G.B. Stracher), Chapter 19; ISBN 978-0-12-849885-9: 409–449; <https://doi.org/10.1016/B978-0-12-849885-9.00013-5>.
- Kruszewski, Ł., Gatel, P., Thiéry, V., Moszumańska, I., Kusy, D., 2018.** Crystallochemical Behavior of Slag Minerals and the Occurrence of Potentially New Mineral Species from Lapanouse-de-Sévérac, France. In: Coal and Peat Fires: A Global Perspective, **5** – “Case Studies – Advances in Field and Laboratory Research” (ed. G.B. Stracher), Chapter 19; ISBN 978-0-12-849885-9: 241–300; <https://doi.org/10.1016/B978-0-12-849885-9.00013-5>
- La Cruz, N.L., Ovale, J.T., Simon, A.C., Konecke, B.A., Barra, F., Reich, M., Leisen, M., Childress, T.M., 2020.** The geochemistry of magnetite and apatite from the El Laco iron oxide-apatite deposit, Chile: Implications for ore genesis. Economic Geology, **115**: 1461–1491; <https://doi.org/10.5382/econgeo.4753>
- Lapidus, A.L., Khudyakov, D.S., Beilina, N.Yu., Trukhina, M.A., Kozlov, A.M., Zhagfarov, F.G., 2022.** Solid fossil fuels as a source of trace elements. Solid Fuel Chemistry, **56**: 1–14; <https://doi.org/10.3103/S0361521922010037>
- Liao, T., Sasaki, T., Sun, Z., 2013.** The oxygen migration in the apatite-type lanthanum silicate with the cation substitution. Physical Chemistry Chemical Physics, **15**: 17552–17559; <https://doi.org/10.1039/C3CP52245H>
- Luo, Y., Hughes, J.M., Rakovan, J., Pan, Y., 2009.** Site preference of U and Th in Cl, F, and Sr apatites. American Mineralogist, **94**: 345–351; <https://doi.org/10.2138/am.2009.3026>
- Machiels, L., Perumal, P., 2022.** (Re)mining Extractive Waste: a new business? Book of abstracts. Romana Origin, ISBN 9789464594966.
- Mao, M., Rukhov, A.S., Rowins, S.M., Spence, J., Coogan, L.A., 2016.** Apatite trace element composition: A robust new method for mineral exploration. Economic Geology, **111**: 1187–1222; <https://doi.org/10.2113/econgeo.111.5.1187>
- Mason, B., Graham, A.L., 1970.** Minor and trace elements in meteoritic minerals. Smithsonian Contributions to the Earth Sciences, **3**: 1–17; [https://doi.org/10.1016/0016-7037\(73\)90081-1](https://doi.org/10.1016/0016-7037(73)90081-1)
- Mazza, D., Tribaudino, M., Delmastro, A., Lebeck, B., 2000.** Synthesis and neutron diffraction study of La<sub>5</sub>Si<sub>2</sub>BO<sub>13</sub>, an analog of the apatite mineral. Journal of Solid State Chemistry, **155**: 389–393; <https://doi.org/10.1006/jssc.2000.8929>
- Mercer, C.N., 2019.** Apatite trace element geochemistry and cathodoluminescent textures – A comparison between regional magmatism and the Pea Ridge IOAREE and Boss IOCG deposits, southeastern Missouri iron metallogenic province, USA. Ore Geology Reviews, **116**: 103129; <https://doi.org/10.1016/j.oregeorev.2019.103129>
- Moore, R.C., Holt, K., Zhao, H., Hasan, A., Awwad, N., Gasser, M., Sanchez, C., 2009.** Sorption of Np(V) by synthetic hydroxyapatite. Radiochimica Acta, **91**: 721–727; <https://doi.org/10.1524/ract.91.12.721.23417>
- Pan, Y., Fleet, M.E., 2002.** Compositions of the apatite-group minerals: substitution mechanisms and controlling factors. Reviews in Mineralogy and Geochemistry, **48**: 13–49; <https://doi.org/10.2138/rmg.2002.48.2>
- Pan, L.-C., Hu, R.-Z., Oyebamiji, A., Wu, H.-Y., Li, J.-W., Li, J.-X., 2021.** Contrasting magma compositions between Cu and Au mineralized granodiorite intrusions in the Tongling ore district in South China using apatite chemical composition and Sr-Nd isotopes. American Mineralogist (Revision 3); <https://doi.org/10.2138/am-2021-7497>
- Parzentny, H., 2020.** spatial macroscale variability of the role of mineral matter in concentrating some trace elements in bituminous coal in a coal Basin – A case study from the Upper Silesian Coal Basin in Poland. Minerals, **10**: 422; <https://doi.org/10.3390/min10050422>
- Pasero, M., Kampf, A.R., Ferraris, C., Pekov, I.V., Rakovan, J., White, T.J., 2010.** Nomenclature of the apatite supergroup min-

- erals. *European Journal of Mineralogy*, **22**: 163–179; <https://doi.org/10.1127/0935-1221/2010/0022-2022>
- Pauling, L., 1961.** The Nature of Chemical Bond. Application of Results Obtained. *Journal of the American Chemical Society*. Ithaca, Cornell University Press; <http://abulafia.mt.ic.ac.uk/shannon/radius.php>; <https://doi.org/>
- Pluta, I., Marcol, A., Bąk, W., 2000.** Siarczany w skałach i wodach kopalni "Marcel" w świetle badań izotopowych (in Polish). *Zeszyty Naukowe Politechniki Śląskiej - Seria Górnictwo*, **247** (1480): 397–405; <https://doi.org/10.5772/62213>
- Ptáček, P., 2016.** Substituents and Dopants in the Structure of Apatite. In: *Apatites and Their Synthetic Analogues, Synthesis, Structure, Properties and Applications* (ed. P. Ptáček), Chapter 6: 289–334; doi:10.5772/62213
- Reifenstein, A.P., Kahraman, H., Coin, C.D.A., Calos, N.J., Miller, G., Uwins, P., 1999.** Behaviour of selected minerals in an improved ash fusion test: quartz, potassium feldspar, sodium feldspar, kaolinite, illite, calcite, dolomite, siderite, pyrite and apatite. *Fuel*, **78**: 1449–1461; [https://doi.org/10.1016/S0016-2361\(99\)00065-4](https://doi.org/10.1016/S0016-2361(99)00065-4)
- Rigali, M.J., Brady, P.V., Moore, R.C., 2016.** Radionuclide removal by apatite. *American Mineralogist*, **101**: 2611–2619; <https://doi.org/10.2138/am-2016-5769>
- Rocha, J., Brandão, P., Lin, Z., Kharlamov, A., Anderson, M.W., 1996.** Novel microporous titanium-niobium-silicates with the structure of nenadkevichite. *Chemical Communications*, **5**: 669–670; <https://doi.org/10.1039/CC9600000669>
- Romero, M., Padilla, I., Contreras, M., López-Delgado, A., 2021.** Mullite-based ceramics from mining waste: a review. *Minerals*, **11**: 332; <https://doi.org/10.3390/min11030332>
- Sader, M.S., Lewis, K., Soares, G.A., LeGeros, R.Z., 2013.** Simultaneous incorporation of magnesium and carbonate in apatite: effect on physico-chemical properties. *Materials Research*, **16**: 779–784; <https://doi.org/10.1590/S1516-14392013005000046>
- Sahasrabudhe, G.S., Krizan, J.W., Bergman, S.K., Cava, R.J., Schwartz, J., 2016.** Million-fold increase of the conductivity in TiO<sub>2</sub> rutile through 3% niobium incorporation. *Chemical Mineralogy*, **28**: 4; <https://doi.org/10.1021/acs.chemmater.6b02031>
- Schleicher, H., 2019.** In-situ determination of trace element and REE partitioning in a natural apatite-carbonatite melt system using Synchrotron XRF Microprobe Analysis. *Journal of the Geological Society of India*, **93**: 305–312; <https://doi.org/10.1007/s12594-019-1178-9>
- Seredin, V.V., Finkelman, R.B., 2008.** Metalliferous coals: a review of the main genetic and geochemical types. *International Journal of Coal Geology*, **76**: 253–289; <https://doi.org/10.1016/j.coal.2008.07.016>
- Serre, C.M., Papiillard, M., Chavassieux, P., Voegel, J.C., Boivin, G., 1998.** Influence of magnesium substitution on a collagen-apatite biomaterial on the production of a calcifying matrix by human osteoblasts. *Journal of Biomedical Materials Research*, **42**: 626–633; [https://doi.org/10.1002/\(sici\)1097-4636\(19981214\)42:4<626::aid-jbm20>3.0.co;2-s](https://doi.org/10.1002/(sici)1097-4636(19981214)42:4<626::aid-jbm20>3.0.co;2-s)
- Sha, L.-K., Chappell, B.W., 1999.** Apatite chemical composition, determined by electron microprobe and laser-ablation inductively coupled plasma mass spectrometry, as a probe into granite petrogenesis. *Geochimica et Cosmochimica Acta*, **63**: 3861–3881; [https://doi.org/10.1016/S0016-7037\(99\)00210-0](https://doi.org/10.1016/S0016-7037(99)00210-0)
- Shannon, R.D., 1976.** Revised effective ionic radii and systematic studies of interatomic distances in halides and chalcogenides. *Acta Crystallographica A*, **32**: 751–767; <http://abulafia.mt.ic.ac.uk/shannon/radius.php>; <https://doi.org/10.1107/S056773947601551>
- Simoes, M.C., Hughes, K.J., Ingham, D.B., Ma, L., Pourkashanian, M., 2017.** Estimation of the Thermochemical Radii and Ionic Volumes of Complex Ions. *Inorganic Chemistry*, **56**: 7566–7573; <https://doi.org/10.1021/acs.inorgchem.7b01205>
- Simpson, D.R., 1968.** Substitutions in apatite: I. Potassium-bearing apatite. *The American Mineralogist*, **53**: 432–444.
- Sokolova, E.V., Pautov, L.A., 1995.** Crystal structure of dusmatovite. *Soviet Physics – Doklady*, **40**: 503–506.
- Ternane, R., Cohen-Adad, M.Th., Panczer, G., Goutaudier, C., Kbir-Arquiub, N., Trabelsi-Ayedi, M., Florian, P., Massiot, D., 2002.** Introduction of boron in hydroxyapatite: synthesis and structural characterization. *Journal of Alloys and Compounds*, **333**: 62–71; [https://doi.org/10.1016/S0925-8388\(01\)01558-4](https://doi.org/10.1016/S0925-8388(01)01558-4)
- Terra, J., Dourado, E.R., Eon, J.-G., Ellis, D.E., Gonzalez, G., Malta Rossi, A., 2009.** The structure of strontium-doped hydroxyapatite: an experimental and theoretical study. *Physical Chemistry Chemical Physics*, **11**: 568–577; <https://doi.org/10.1039/b802841a>
- Tollari, N., Barnes, S.-J., Cox, R.A., Nabil, H., 2008.** Trace element concentrations in apatites from the Sept-Îles Intrusive Suite, Canada – Implications for the genesis of nelsonites. *Chemical Geology*, **252**: 180–190; <https://doi.org/10.1016/j.chemgeo.2008.02.016>
- Tunheng, A., Hirata, T., 2004.** Development of signal smoothing device for precise elemental analysis using laser ablation-ICP-mass spectrometry. *Journal of Analytical Atomic Spectroscopy*, **19**: 932–934; <https://doi.org/10.1039/B402493A>
- van Achterbergh E., Ryan, C.G., Jackson, S.E., Griffin, W.L., 2001.** Data reduction software for LA-ICP-MS. In: *Sylvester PJ (ed) Laser ablation-ICPMS in the earth sciences: principles and applications*. Mineralogical Association of Canada, Ottawa, Ontario, Canada: 239–243; <https://doi.org/10.1180/002646102753705408>
- Villiars, P., Cenzual, K., Gladyshevskii, R., 2015.** Handbook of Inorganic Substances. De Gruyter, Berlin, Germany; <https://doi.org/10.1107/S2053229616010172>
- Vrancken, K., Delgado, R., 2016.** EIT Raw Materials needs and opportunities for Copernicus products and services; <http://www.copernicus.eu> (Retrieved 10.11.2022)
- Wang, J., Lian, J., Gao, F., 2015.** Radionuclide incorporation and long term performance of apatite waste forms 11-3105. Project, Fuel Cycles, U.S. Department of Energy, RCS Advances, 3, 15178; <https://doi.org/10.2172/1248954>
- Wang, T.J., ZhiLi, D., 2003.** Structural derivation and crystal chemistry of apatites. *Acta Crystallographica B*, **59**: 1–16; <https://doi.org/10.1107/s0108768102019894>
- Warner, N.R., Darrah, T.H., Jackson, R.B., Millot, R., Kloppmann, W., Vengosh, A., 2014.** New tracers identify hydraulic fracturing fluids and accidental releases from oil and gas operations. *Environmental Science and Technology*, **48**: 12552–12560; <https://doi.org/10.1021/es5032135>
- Wiesmann, H.-P., Plate, U., Zierold, K., Höhling, H.J., 1998.** Potassium is involved in apatite biomineralization. *Journal of Dental Restoration*, **77**: 1654–1657; <https://doi.org/10.1177/00220345980770081401>
- Xiqiang, L., Hui, Z., Yong, T., Yunlong, L., 2020.** REE geochemical characteristics of apatite: implications for ore genesis of the Zhijin Phosphorite. *Minerals*, **10**: 1012; <https://doi.org/10.3390/min10111012>
- Xu, B., Kou, G., Etschmann, B., Liu, D., Brugger, J., 2020.** Spectroscopic, EMPA, Micro-XRF and Micro-XANES analyses of sulphur concentration and oxidation state of natural apatite crystals. *Crystals*, **10**: 1032; <https://doi.org/10.3390/cryst10111032>
- Yakymchuk, C., 2017.** Behaviour of apatite during partial melting of metapelites and consequences for prograde suprasolidus monazite growth. *Lithos*, **274–275**: 412–426; <https://doi.org/10.1016/j.lithos.2017.01.009>
- Yokota, T., Honda, M., Aizawa, M., 2017.** Fabrication of potassium-substituted hydroxyapatite ceramics via ultrasonic spray-pyrolysis route. *Phosphorus Research Bulletin*, **33**: 35–40; <https://doi.org/10.3363/prb.33.35>
- Zhang, Y., Tan, H., Cong, P., Rao, W., Ta, W., Lu, S., Shi, D., 2022.** Boron and lithium isotopic constraints on their origin, evolution, and enrichment processes in a river – groundwater – salt lake system in the Qaidam Basin, northeastern Tibetan Plateau. *Ore Geology Reviews*, **149**: 105110; <https://doi.org/10.1016/j.oregeorev.2022.105110>
- Zhang, P., Li, W., White, N.C., Zhang, L., Qiao, X., Yao, Z., 2020.** Geochemical and isotopic study of metasomatic apatite: Implications for gold mineralization in Xindigou, northern China. *Ore Geology Reviews*, **127**: 103853; <https://doi.org/10.1016/j.oregeorev.2020.103853>

## APPENDIX 1

Comparison of ionic (thermochemical) radii of anions (Jenkins and Thakur, 1979; Simoes et al., 2017) and cations (Pauling, 1961; Shannon, 1976), the radii are shown as calculated geometric means from published data

